# Flexible Simulation Based Inference for Galaxy Photometric Fitting with Synthesizer

Thomas Harvey<sup>1\*</sup>, Christopher C. Lovell<sup>2,3</sup>, Sophie Newman<sup>4</sup>, Christopher J. Conselice<sup>1</sup>, Duncan Austin<sup>1</sup>, William J. Roper<sup>5</sup>, Aswin P. Vijayan<sup>5</sup>, Stephen M. Wilkins<sup>5</sup>, Patricia Iglesias-Navarro<sup>6,7</sup>, Vadim Rusakov<sup>1</sup>, Qiong Li<sup>1</sup>, Nathan Adams<sup>1</sup>, Kai Magdwick<sup>1</sup>, and Matthew Ho<sup>8</sup>

<sup>1</sup>Jodrell Bank Centre for Astrophysics, University of Manchester, Oxford Road, Manchester M13 9PL, UK

Accepted XXX. Received YYY; in original form ZZZ

# ABSTRACT

We introduce synference, a new, flexible Python framework for galaxy SED fitting using simulation-based inference (SBI). Synference leverages the synthesizer package for flexible forward-modelling of galaxy SEDs and integrates the Ltu-ILI package to ensure best practices in model training and validation. In this work we demonstrate synference by training a neural posterior estimator on 10<sup>6</sup> simulated galaxies, based on a flexible 8-parameter physical model, to infer galaxy properties from 14-band HST and JWST photometry. We validate this model, demonstrating excellent parameter recovery (e.g. R<sup>2</sup> >0.99 for M<sub>\*</sub>) and accurate posterior calibration against nested sampling results. We apply our trained model to 3,088 spectroscopically-confirmed galaxies in the JADES GOODS-South field. The amortized inference is exceptionally fast, having nearly fixed cost per posterior evaluation and processing the entire sample in ~3 minutes on a single CPU (18 galaxies/CPU/sec), a ~1700× speedup over traditional nested sampling or MCMC techniques. We demonstrate synference's ability to simultaneously infer photometric redshifts and physical parameters, and highlight its utility for rapid Bayesian model comparison by demonstrating systematic stellar mass differences between two commonly used stellar population synthesis models. synference is a powerful, scalable tool poised to maximise the scientific return of next-generation galaxy surveys.

Key words: methods: data analysis – techniques: photometric – galaxies: photometry – galaxies: stellar content

# 1 INTRODUCTION

Current and future space and ground-based surveys by missions including the James Webb Space Telescope (Gardner et al. 2006), Euclid (Euclid Collaboration et al. 2025), the Nancy Grace Roman Space Telescope (Spergel et al. 2015), the Vera C. Rubin Observatory (Ivezić et al. 2019) and SPHERE-X (Doré et al. 2014), among others, will cumulatively observe > 20 billion galaxies in the next decade. The unprecedented precision and volume of this data necessitate the development of increasingly sophisticated and performant models to interpret the diverse range of observed galaxy properties. Constraining these models is therefore a critical step towards a more complete understanding of galaxy formation and evolution. However, conventional Bayesian techniques for posterior parameter inference, such as Markov Chain Monte Carlo or nested sampling, are computationally prohibitive for such large-scale analyses. Inference for

A promising solution to this scalability challenge is *simulation-based inference* (SBI), also known as *likelihood-free inference* and

<sup>&</sup>lt;sup>2</sup>Kavli Institute for Cosmology, Madingley Road, Cambridge CB3 0HA, UK

<sup>&</sup>lt;sup>3</sup>Institute of Astronomy, Madingley Road, Cambridge CB3 0HA, UK

<sup>&</sup>lt;sup>4</sup>Institute of Cosmology and Gravitation, University of Portsmouth, Burnaby Road, Portsmouth PO1 3FX, UK

<sup>&</sup>lt;sup>5</sup>Astronomy Centre, University of Sussex, Falmer, Brighton BN1 9QH, UK

<sup>&</sup>lt;sup>6</sup>Instituto de Astrofísica de Canarias, C/ Vía Láctea s/n, 38205 La Laguna, Tenerife, Spain

<sup>&</sup>lt;sup>7</sup>Departamento de Astrofísica, Universidad de La Laguna, 38200 La Laguna, Tenerife, Spain

<sup>&</sup>lt;sup>8</sup>Department of Astronomy, Columbia University, New York, NY 10027, USA

a single galaxy can require anywhere from minutes (e.g. BAGPIPES; Carnall et al. 2017) to several days (e.g. PROSPECTOR; Johnson et al. 2020; Tacchella et al. 2022) of CPU time, depending on model complexity and forward model efficiency, rendering these methods orders of magnitude too slow for these forthcoming datasets. As a result, there have been numerous approaches to improving the speed of SED fitting using a variety of machine learning methods. One approach is to emulate the simulator using a neural network emulator (Alsing et al. 2020; Mathews et al. 2023), whilst other approaches have utilized approaches including manifold learning (Hemmati et al. 2019; Davidzon et al. 2022; Asadi et al. 2025), de-noising autoencoders (Frontera-Pons et al. 2017), Convolutional Neural Networks (Lovell et al. 2019; Dobbels et al. 2019; Surana et al. 2020), and Natural Gradient Boosting (Gilda et al. 2021). These approaches typically produce only a point parameter estimate, rather than a full posterior, and can be quite sensitive to the training dataset used.

<sup>\*</sup> E-mail: thomas.harvey-3@manchester.ac.uk

implicit likelihood inference (Cranmer et al. 2020). SBI methods circumvent the need for an explicit likelihood function, Instead learning a statistical mapping between observations and data based on Bayesian statistics. The SBI approach utilizes a neural network as a Neural Density Estimator (NDE), which is trained to predict the posterior (Neural Posterior Estimation), likelihood (Neural Likelihood Estimation), or the likelihood-to-evidence ratio (Neural Ratio Estimation). A key advantage of SBI, and NPE in particular, is its capacity for amortized posterior estimation. Once a neural network is trained on a comprehensive set of simulations, it can generate posterior distributions for new observations almost instantaneously, without requiring any further optimization. This amortized nature enables efficient scaling to the vast datasets produced by upcoming surveys. Furthermore, the resulting posterior distributions capture the full uncertainty landscape, including parameter degeneracies, which is a significant advantage over optimisation methods that yield only point estimates, such as  $\chi^2$  minimisation.

In recent years, SBI has been successfully applied across a range of astrophysical and cosmological contexts. For individual galaxies, applications include spectral energy distribution (SED) fitting with photometry/spectroscopy (Hahn & Melchior 2022; Khullar et al. 2022; Wang et al. 2023c; Fischbacher et al. 2025), star formation history (SFH) reconstruction from photometry and spectroscopy (Aufort et al. 2024; Iglesias-Navarro et al. 2024), decomposition of active galactic nuclei (AGN) from their host galaxies (Berger et al. 2025; Yuan et al. 2025), and inference of galaxy dynamics (Widmark & Johnston 2025; Sante et al. 2025; Brooks et al. 2025). The technique has also been extended to spatially-resolved SED fitting (Iglesias-Navarro et al. 2025). On larger scales, SBI has been used to infer dark matter halo properties (Hahn et al. 2024), the history of cosmic reionization (Chen et al. 2023; Choustikov et al. 2025), and high-dimensional parameters of population-level models (Lovell et al. 2024; Moser et al. 2024; Li et al. 2024; Thorp et al. 2024, 2025; Gunes et al. 2025; Deger et al. 2025). SBI is also used extensively within cosmology for parameter inference (e.g. Alsing et al. 2019; Modi et al. 2023; Mediato-Diaz & Handley 2025; Zubeldia et al. 2025; Jeffrey et al. 2025).

In this work, we present SYNFERENCE, a new, flexible SBI framework designed for robust galaxy SED fitting. SYNFERENCE leverages the SYNTHESIZER package (Lovell et al. 2025; Roper et al. 2025) for the flexible creation of training data and integrates the LTU-ILI package (Ho et al. 2024) to ensure best practices in model configuration, training, and validation. To demonstrate its capabilities, we apply SYNFERENCE to infer the physical properties of galaxies from the JWST Advanced Deep Extragalactic Survey (JADES, Eisenstein et al. 2023a; Rieke et al. 2023a), using a combination of JWST and Hubble Space Telescope (HST) photometry.

The paper is structured as follows. In Section 2, we provide a technical overview of SBI methods. In Section 3 we provide an overview of the SYNFERENCE framework. Section 4 details the generation of our training data and the model training process, followed by a thorough evaluation of the trained model in Section 4.4. We apply our framework to the JADES dataset in Section 5. In Section 6, we discuss the limitations of our model, compare our results with those in the literature, and outline future directions. Finally, we summarize our findings in Section 7.

Throughout this paper, we assume a standard  $\Lambda$ CDM cosmology with  $H_0 = 70 \text{ km s}^{-1} \text{ Mpc}^{-1}$ ,  $\Omega_{\text{M}} = 0.3$  and  $\Omega_{\Lambda} = 0.7$ .

# 2 SIMULATION-BASED INFERENCE

This section briefly reviews key concepts of simulation-based inference. SBI is a class of machine learning techniques for performing parameter inference in scenarios where the underlying physical process can be simulated but the likelihood function is analytically intractable or computationally prohibitive to evaluate. In many scientific domains, it is straightforward to construct a stochastic simulator that executes the "forward problem": predicting an observation x given a set of model parameters  $\theta$ . However, scientific inquiry typically requires solving the "inverse problem": inferring the posterior probability distribution of the parameters given an observation,  $p(\theta|x_i)$ ,

According to Bayes' theorem, the posterior is given by:

$$p(\theta|x_i) = \frac{p(x_i|\theta)p(\theta)}{p(x_i)} \tag{1}$$

where  $p(\theta)$  is the *prior* distribution of the parameters,  $p(x_i|\theta)$  is the *likelihood* and  $p(x_i)$  is the *marginal likelihood* or *evidence*. SBI methods bypass the need for an explicit likelihood function by instead learning the statistical relationship between parameters and observations from a training set of simulated observation-parameter pairs,  $\mathcal{D} = \{(x_i, \theta_i)\}_{i=1}^N$ .

To achieve this, SBI leverages a technique called neural density estimation (Papamakarios et al. 2018), where a neural network is trained to approximate a conditional probability distribution. Depending on which component of Bayes' theorem is approximated, SBI methods can be broadly categorized.

#### 2.1 Neural Posterior Estimation

In Neural Posterior Estimation (NPE), the network directly learns the posterior distribution  $p(\theta|x)$  (Greenberg et al. 2019). This is achieved by training a conditional probability distribution,  $q_{\phi}(\theta|x)$ , (where  $\phi$  represents the network weights) to approximate the true posterior. The training process typically minimizes the Kullback-Leibler (KL) divergence (Kullback & Leibler 1951) between the learned and true posteriors, averaged over all simulated data.

$$D_{\text{KL}}(p||q) = \int p(\theta|x) \log \frac{p(\theta|x)}{q_{\phi}(\theta|x)} d\theta$$
 (2)

We can define a loss function L by taking the expectation  $\mathbb{E}_{p(x)}$  over the training dataset  $\mathcal{D}$ , for which an optimizer (e.g. Adam Kingma & Ba 2014) is used to minimize the gradient of L with respect to the network parameters.

$$\mathcal{L} = \mathbb{E}_{p(x)} D_{KL} = \mathbb{E}_{p(x,\theta)} \left[ -\log q_{\phi}(\theta|x) \right]$$
 (3)

In practice, this loss function encourages the network to maximize the probability of the true parameters  $\theta_i$  that correspond to each simulated observation  $x_i$  in the training set.

A large number of different model architectures have been used to represent the conditional probability distribution  $q(\theta|x)$ . There are two major categories which are commonly used; **normalising flow** (NF, Kobyzev et al. 2021; Papamakarios et al. 2021) models and **mixture density networks** (MDN, Bishop 1994). MDNs are a neural architecture where the conditional probability distribution is represented by a mixture model with learned weights and biases. Normalising flow architectures, such as **Masked Autoregressive Flows** (Papamakarios et al. 2018) and **Neural Spine Flows** (Papamakarios et al. 2021), use invertible transformations of a base Gaussian

distribution to represent complex conditional probability distributions using a neural network. Alternative approaches, such as using transformer-based diffusion models, have also shown promising performance (Thorp et al. 2024, 2025; Gloeckler et al. 2024).

Other SBI families include Neural Likelihood Estimation (NLE) (Papamakarios et al. 2019), which learns the likelihood  $p(x|\theta)$  and Neural Ratio Estimation (NRE), which learns a likelihood ratio (Hermans et al. 2020; Durkan et al. 2020). While powerful, both NLE and NRE require an additional sampling step (e.g., MCMC) to generate posteriors for a given observation, making them less computationally performant than NPE for the large-scale applications motivating this work. Therefore, we primarily focus on the NPE method in this study, although synference does support NLE and NRE, as well as the sequential variants (SNPE, SNLE, SNRE), where multiple rounds of training are performed.

# 2.2 Strengths of SBI

SBI, and particularly NPE, offers several key advantages over traditional inference techniques:

- (i) **Amortized Inference:** Once an NPE model is trained, generating posterior samples for a new observation is computationally trivial. This "amortization" of the inference cost across all possible observations means that analysing millions of galaxies becomes feasible, as the expensive training phase is performed only once.
- (ii) **Full Posterior Characterization:** Unlike optimisation methods that yield only a single best-fit point estimate (e.g., a maximum likelihood value), SBI provides the full posterior distribution. This captures all parameter uncertainties and degeneracies, providing a more complete and robust picture of the inference result.
- (iii) **Likelihood-Free:** SBI is applicable to any scientific model from which one can forward-simulate data. This flexibility allows for the use of highly complex and realistic simulators for which an analytical likelihood is unknown. In the context of SED fitting this allows utilization of e.g. forward-modelled hydrodynamical simulation outputs as the training dataset directly (e.g. Choustikov et al. 2025).
- (iv) **Model Comparison:** SBI techniques can be leveraged for Bayesian model comparison either by learning the posterior and likelihood (Spurio Mancini et al. 2023) or directly training a neural network classifier to predict the Bayes factor between two competing models (Jeffrey & Wandelt 2024). Alongside the speed of inference these techniques make SBI a competitive tool for Bayesian model selection.

# 2.3 Practical Considerations and Challenges

While powerful, the application of SBI requires careful consideration of its implementation, potential challenges, and validation. In this section we briefly outline and discuss these challenges in the context of SED fitting.

# 2.3.1 SBI Implementation

A number of open-source Python packages have been developed to streamline the implementation of SBI. Notable examples include SBI (Tejero-Cantero et al. 2020), LAMPE (Boelts et al. 2024), and PYDELFI (Alsing et al. 2019), as well as newer approaches (e.g. SIMFORMER) implementing novel architectures such as transformers (Gloeckler et al. 2024). These packages are built on top of the machine learning and GPU acceleration frameworks PyTorch, Tensorflow and JAX

(Paszke et al. 2019; Developers 2022; Bradbury et al. 2021). The L<sub>T</sub>U-ILI package (Ho et al. 2024) further unifies several of these tools into a cohesive framework and implements consistent best practices for model evaluation. In this paper we use LtU-ILI with the *sbi* backend for our fiducial model.

# 2.3.2 Ongoing Challenges

Several challenges must be addressed when applying SBI to astrophysical problems like SED fitting.

- Expensive Forward Modelling: SBI relies on a library of observation parameter pairs generated through a forward model. Depending on the complexity of the forward model or simulation this can be a significant burden. However emulators which predict the observations given the parameters have also been successfully used to build training datasets for SBI, e.g. SPECULATOR (Alsing et al. 2020) or Parrot (Mathews et al. 2023). Active learning (Griesemer et al. 2024) can also significantly reduce the required library size for specific applications.
- **Designing a training dataset:** The explicit and implicit prior choices in the training dataset will be learned by the model, and these need to be chosen carefully to ensure the model is both applicable and unbiased, as well as precise enough for the intended application. Broad parameter sampling is important for accurate results, and low-dispersion sampling methods such as Latin Hypercube or Sobol Sequence can ensure this whilst reducing the total number of simulations required. The size of the training set required typically scales with the dimensionality of the inference (Bairagi et al. 2025), and typically ranges from 10<sup>4</sup> to 10<sup>6</sup> for parameter inference with 5-10 dimensions.
- Model misspecification: This occurs when the simulator used for training is an imperfect representation of reality, or when an observation lies outside the parameter space covered by the training data (Cannon et al. 2022). Applying a trained model to such "out-of-distribution" data can lead to biased and unreliable posteriors. Methods to detect misspecification include checking for consistency across an ensemble of models (Alvey et al. 2025), using outlier detection algorithms as a prior predictive check (Aufort et al. 2024), or explicitly modelling potential mismatches, as demonstrated by sbi++ (Wang et al. 2023c). Techniques such as Domain Adaption have also been used to enable neural networks to trained on simulated data perform more accurately when applied to real data (e.g. for SDSS galaxies trained on Illustris simulations in Ciprijanović et al. 2021).
- Noise and Uncertainty Modelling: If we wish to apply our trained model to reality, we must model the imperfect measurement process which introduces both systematic and random noise into our observations. Modelling this noise accurately is important for the trained SBI model to perform accurately when applied to real data. In astrophysical observations we often deal with heteroscedastic, non-Gaussian and correlated noise which can be difficult to model, and often differs between different observations and surveys. Various techniques to model noise have been suggested, including de-noising score matching (Vincent 2011), noise-insensitive loss functions (Huber loss), or direct modelling of noise distributions using a trained score-based diffusion model (e.g. Thorp et al. 2025).
- Missing Data: Heterogeneous datasets are common in astronomy, such as missing or incomplete photometric survey coverage in certain filters. Standard 'SBI' approaches, like many ML techniques, require a fixed input data vector of known size. Strategies to handle this include imputing missing values using nearest-neighbour searches in the training set (Wang et al. 2022, 2023c), or condition-

# 4 Harvey et al.

ing the model on the data availability pattern itself by using a binary mask as an additional input (Wang et al. 2024). Architectures that use tokenization and attention mechanisms, such as transformers, are also naturally suited to handling missing data (Gloeckler et al. 2024).

• Sensitivity to Hyperparameters: The computational and posterior predictive performance of an SBI model is sensitive to choices of neural architecture, network size, learning rate, and other training hyperparameters. Finding the optimal configuration often involves navigating a bias-variance trade-off. This process can be automated using optimization frameworks like Optuna (Akiba et al. 2019). Additionally, creating an ensemble of models trained with different hyperparameters can improve robustness and provide more reliable posterior estimates (Hermans et al. 2021), at the cost of more computation.

### 2.3.3 Benchmarking SBI Models

Once the SBI model has been trained, validating model performance is critical to understanding whether the model is accurate and unbiased before it is applied to real observations. This benchmarking should always be performed on a held-out test set to ensure the model generalizes well and is not overfit to the training data (Lueckmann et al. 2021). Commonly used benchmarks for precision include comparison of true vs predicted marginal parameters, producing corner plots showing multivariate distributions of parameter pairs, or the cumulative likelihood of the validation dataset (Ho et al. 2024).

A model can be precise but biased, or it may underestimate the true uncertainty in the posterior distribution. If available, tests against reference posteriors (obtained by nested sampling or MCMC) such as Classifier 2 Sample Tests (C2ST, Lopez-Paz & Oquab 2016) and Probability-Integral Transform (PIT)/Simulation-based calibration (SBC) (Cook et al. 2006; Zhao et al. 2021; Talts et al. 2018) can be used to assess the performance of a model. However reference posteriors are typically computationally expensive, so alternative methods like coverage tests, *Tests of Accuracy with Random Points* (TARP, Lemos et al. 2023), truncated proposals Deistler et al. (2022) can be used to evaluate multivariate and marginal posterior coverage.

# 3 SYNFERENCE: A FLEXIBLE SBI FRAMEWORK FOR SED FITTING

To address the aforementioned issues prevalent in SBI in the context of SED fitting, we introduce synference, a Python package that provides a flexible framework for building, training, and applying SBI models to infer galaxy properties from photometric and spectroscopic observations. With synference we aim to make utilizing SBI approaches for SED fitting more accessible to users without ML experience.

SYNFERENCE is designed to provide flexibility to the user in every stage, which we have conceptually split into distinct stages:

(i) **Simulation**: A forward model is used to generate a comprehensive library of simulated observations (x) and their corresponding physical parameters ( $\theta$ ). By default, SYNFERENCE uses SYNTHESIZER for this stage, but it is also compatible with models from other SED modelling codes (e.g., BAGPIPES, PROSPECTOR) or forward modelled emission from cosmological models, e.g. hydrodynamic simulations such as EAGLE (Schaye et al. 2015; Crain et al. 2015) and IllustrisTNG (Pillepich et al. 2018)). More generally, any simulator which

predicts astrophysical observables given some parameters, for example output emission from radiative transfer modelling codes (e.g., SKIRT Camps & Baes 2015), Stellar Population Synthesis (SPS) codes (e.g., FSPS, BPASS, Conroy & Gunn 2010; Stanway & Eldridge 2018)), photoionization modelling codes (CLOUDY, Ferland et al. 2017) can all in theory used to train a model using SYNFERENCE.

- (ii) **Feature Engineering**: The raw simulation library is processed to create a training-ready dataset. This involves selecting specific observables (e.g., photometric filters, wavelength range/resolution), applying realistic noise models, and performing data transformations to ensure numerical stability during training.
- (iii) **Training and Validation**: An SBI model is trained on the engineered feature set. Through its LTU-ILI backend, SYNFERENCE supports a wide variety of neural density estimators for NPE, NLE, and NRE, with hyperparameter optimisation provided by OPTUNA. Model performance and validation are run by default for every model (e.g. coverage plots, rank histogram, parameter metrics, TARP, training loss, multivariate corner plots for posteriors, and log probability distributions). This makes it easy for the end-user to assess the performance and applicability of their trained model.
- (iv) **Inference**: The trained model is applied to real observational data. This stage includes automated data transformations, prior predictive checks to flag model misspecification, and built-in tools for posterior visualization.

A key design principle of SYNFERENCE is the decoupling of the simulation and training stages. This modularity allows a single, comprehensive library of simulated SEDs to be reused for training multiple SBI models, each tailored to a specific observational dataset or scientific question. The framework is built for scalability, with MPI support for parallelized data generation on high-performance computing (HPC) systems. SYNFERENCE is publicly available on GitHub<sup>1</sup>. A schematic of the overall workflow is shown in Figure 1, highlighting the process of constructing, building and training a model using SYNFERENCE.

# 3.1 The Forward Model: synthesizer

The foundation of any SBI application is a high-fidelity forward model. SYNFERENCE leverages SYNTHESIZER (Lovell et al. 2025; Roper et al. 2025), a Python package for generating synthetic galaxy observations. SYNTHESIZER can produce complex, multi-component SEDs incorporating stellar continuum, nebular emission (using the photoionization code CLOUDY, Ferland et al. 2017), dust attenuation and emission, AGN emission, and intergalactic medium (IGM) absorption. It supports a wide range of SPS models, initial mass functions (IMFs), star formation histories, and dust laws, as summarized in Table 1. This flexibility allows users to construct bespoke physical models tailored to their specific scientific goals. One of the unique approaches of SYNTHESIZER is the unified approach to forward modelling from both parametric models and outputs of hydrodynamical simulations, allowing like-for-like comparisons between inverse and forward modelling approaches.

Throughout the rest of this paper we adopt a number of fiducial modelling choices for the purposes of demonstrating the SYNFERENCE framework, which we call Model 1. We model the stellar emission using the BPASS v2.2.1 SPS grids (Stanway & Eldridge 2018), assuming a Chabrier & Gilles (2003) IMF with mass limits of 0.1 and  $300M_{\odot}$ . Nebular emission is included assuming a fixed ionization

https://github.com/synthesizer-project/synference

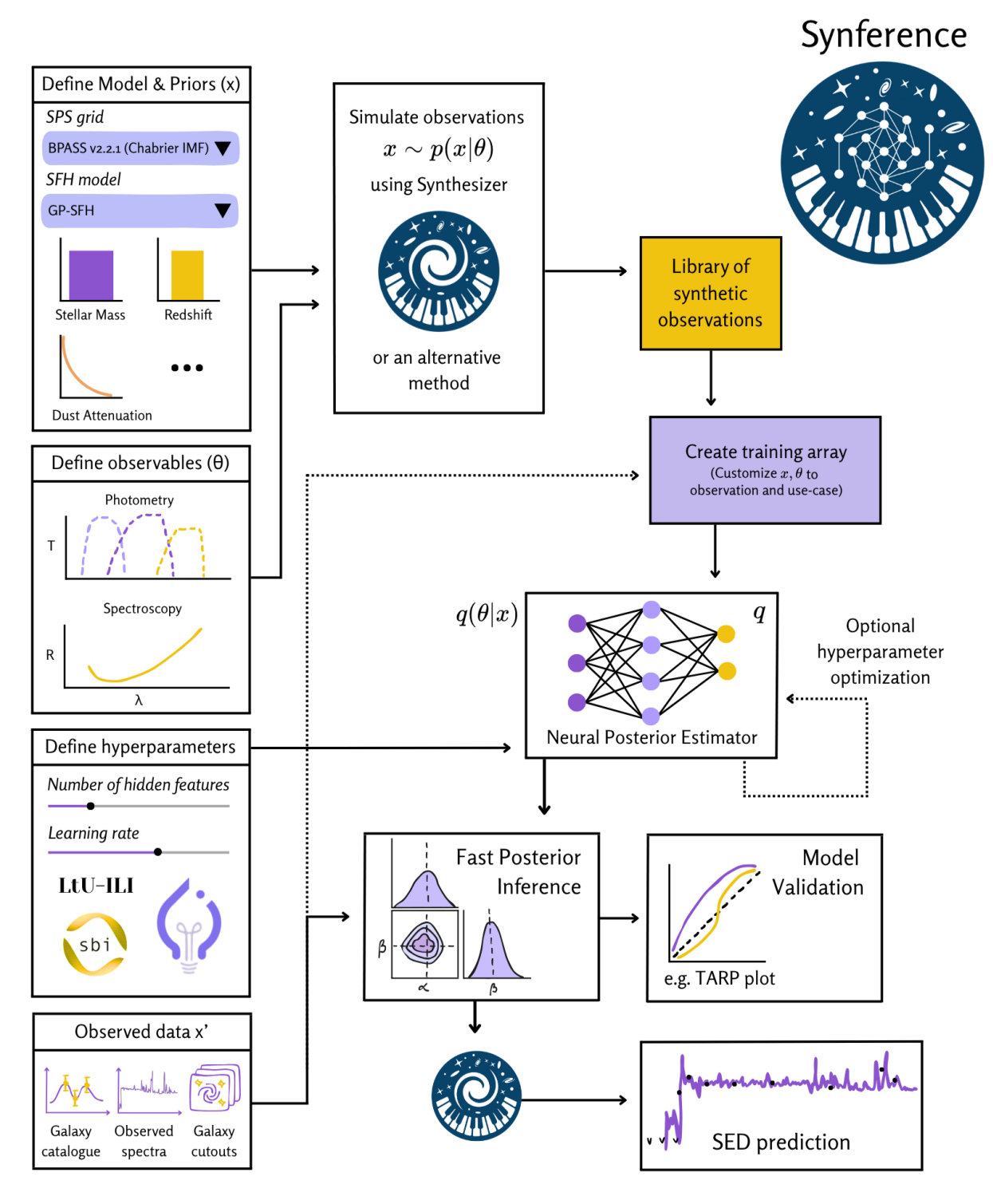


Figure 1. Schematic illustration of the SYNFERENCE workflow. User-defined inputs are shown on the left, including the physical model configuration within SYNTHESIZER, the choice of instrumentation (photometric filters, wavelength range, spectral resolution), as well as the SBI model hyperparameters for the neural density estimator, which utilizes the LTU-ILI package (Ho et al. 2024) with either the SBI (Tejero-Cantero et al. 2020) or LAMPE (Boelts et al. 2024) backends. The SYNFERENCE framework processes these to generate a library of mock observations, either using the SYNTHESIZER package or directly from a user-provided model. From this library we generate a training array for the SBI model, then train a neural density estimator to emulate the posterior or likelihood. The hyperparameters can be optionally optimized using OPTUNA (Akiba et al. 2019). The amortized trained model can then be utilized for direct inference from observed data to generate reliable Bayesian posterior estimates. Optionally these posteriors can be used to reconstruct the predicted SED of the galaxy.

#### SPS Grids

BC03 (Bruzual & Charlot 2003), BPASS (Stanway & Eldridge 2018), FSPS (Conroy & Gunn 2010), Maraston (Maraston 2005; Newman et al. 2025), Yggdrasil (Zackrisson et al. 2011)

#### **Star Formation Histories**

Parametric: Constant, Exponential, Declining Exponential,
Delayed Exponential, Lognormal, Double Powerlaw.

Non-parametric "Continuity", "Continuity Flex" (Leja et al. 2019),

"Continuity PSB" (Suess et al. 2022),

"Dirichlet" (Leja et al. 2017, 2019), Dense Basis (Iyer et al. 2019),

# **Dust Attenuation and Emission**

Attenuation Laws: Powerlaw, Calzetti et al. (2000), Charlot & Fall (2000), Li et al. (2008) [MW, SMC, LMC]. Emission: Blackbody, Greybody, Casey (2012), Draine & Li (2007) IGM Attenuation: Madau (1995); Inoue et al. (2014); Asada et al. (2025)

#### **AGN Modelling**

UNIFIEDAGN: QSOSED (Kubota & Done 2018) model [Torus, NLR, BLR]

parameter of  $\log_{10} U = -2$ . Dust attenuation is modelled with a single-component Calzetti et al. (2000) and dust emission is modelled as a greybody with a fixed temperature of 40K and emissivity  $\beta = 1.5$ , with IR flux density calculated assuming overall energy balance with reprocessed ionizing photons. IGM attenuation is applied using the model of Inoue et al. (2014).

Whilst we make these explicit choices in order to demonstrate SYNFERENCE through Model 1, these decisions can be fully configured by the end user, and SYNTHESIZER offers a very wide variety of options for different use-cases.

On the observation side SYNTHESIZER SUPPORTS all instruments provided by the Spanish Virtual Observatory (SVO; Rodrigo et al. 2012; Rodrigo & Solano 2020), as well as custom filter profiles, so photometry can be generated for any combination of filters. SYNFERENCE also supports inference directly from spectral observations, given that an embedding network is provided to reduce the dimensionality of the observations. Whilst detailed applications to spectroscopy are beyond the scope of this work, we plan to explore this functionality of SYNFERENCE in future work.

# 3.1.1 Star Formation History Parametrizations

A significant number of star-formation history parametrizations have been suggested in the literature to represent the complex and diverse growth of stellar populations. SFH timescales can vary significantly between galaxies, from stochastic bursts on Myr timescales in low-mass galaxies to smoothly varying across Gyr timescales in massive quiescent galaxies (Iyer et al. 2020). Representing these diverse shapes and timescales of variability with a simple model is an ongoing challenge.

Proposed models broadly fall into two groups; 'parametric' models, typically represented by smoothly time-varying functions such as a 'delayed' or 'declining' exponential, or a more complex lognormal or double power-law model (Carnall et al. 2019), and 'non-parametric' models, where a SFH is represented by a time-binned or stochastic process, such as the 'continuity' model of Leja et al. (2019); Tacchella et al. (2022), the 'Dense Basis' model of Iyer et al. (2019), or the stochastic SFH power-spectrum prior of Wan et al. (2024) (see also Iyer et al. 2024). The 'non-parametric' models typically have more degrees of freedom than parametric models but may better represent the diversity of observed SFHs, although care must

be taken to select appropriate hyperparameters and priors for these models.

Through SYNTHESIZER, SYNFERENCE supports many common parametric and 'non-parametric' SFHs, as listed in Table 1, and users can also simply add additional models as desired. For <code>Model 1</code> we implement a flexible Gaussian-process-based SFH from Iyer et al. (2019), where the SFH is controlled by a decoupled recent SFR and N=3 parameters controlling the lookback time at which 25/50/75% of the total stellar mass formed ( $t_{25}$ ,  $t_{50}$ ,  $t_{75}$ ). The prior on these parameters takes the form of a Dirichlet distribution, for which we set  $\alpha=1$ , which controls the correlation of the parameters and the condition  $t_{25} < t_{50} < t_{75}$ . Whilst increasing the number of parameters would allow for more complex star formation histories, it also becomes more difficult for the neural network to recover the true star formation history, particularly when attempting to infer it from photometric observations.

### 3.2 Simulating mock observations

We list our prior parameters and their allowed ranges for Model 1 in Table 2. Using the Model 1 simulator, we generate a large training dataset by sampling from the prior distributions defined in Table 2. We adopt broad, non-informative uniform or log-uniform priors for our free parameters to ensure the training set covers a wide hypervolume of galaxy properties. We impose a sSFR prior to cover a range of sSFR values, but we choose to infer log<sub>10</sub> SFR directly rather than the specific star formation rate. The free parameters in Model 1 are: stellar mass  $M_{\star}$ , V-band dust attenuation  $(A_{\rm V})$ , stellar metallicity  $(Z_{\star})$ , star formation rate (SFR), and the three SFH parameters ( $t_{25}$ ,  $t_{50}$ ,  $t_{75}$ ), for a total of seven free parameters. For each simulated observation we also calculate several derived parameters which we can train the model to infer directly, including mass-weighted age, star-formation rates averaged over several timescales, UV  $\beta$  slope and the surviving stellar mass calculated from the SPS return fractions given the SFH and metallicity.

The size of the training dataset required for a robust posterior estimator depends on the dimensionality of the inference problem and the neural network architecture. Higher dimensional models will need significantly larger training datasets to provide adequate sampling of the parameter volume. For models in the literature with comparable dimensionality these can range from  $10^4$  to a few  $\times 10^6$ ; Choustikov et al. (2025) use only 13,800 high-fidelity observations (forward modelled photometry from the SPHINX simulation), whilst Iglesias-Navarro et al. (2025) used  $10^6$  and Wang et al. (2024) used  $\approx 2 \times 10^6$ . To ensure efficient coverage of the parameter space, we use Latin Hypercube (LHC) sampling (McKay et al. 2000). For our 8-parameter problem, we generate models with both  $10^5$  and  $10^6$  samples, which we utilize in later sections for different purposes.

For each parameter sample, we use SYNTHESIZER to compute the full SED and derive noiseless observer-frame photometry in a wide range of HST (ACS, WFC3/IR) and JWST (NIRCam, MIRI) filters. The noise is not added at this stage; instead, it is applied dynamically during the feature engineering phase, allowing the same base library to be used for applications to surveys with different depths. The entire generation process can be parallelized using MPI over multiple HPC nodes and the outputs are stored in a series of compressed HDF5 files, in a standardised and self-documented format. By simply importing an MPI python package and running with mpirun this can easily be distributed over HPC resources, with no additional user configuration required.

**Table 2.** Free and fixed parameter values and priors for Model 1. The upper table shows the varying parameters and their associated prior distributions, along with a brief description. The lower table shows the fixed values for other parameters assumed for Model 1. A  $^{\dagger}$  means that for Model 1 this parameter is provided as a input feature to the model.

	Parameter	$Prior \in [Value/Range]$	Description	
Fixed parameters Free parameters	$z^{\dagger}$	Uniform ∈ [0, 14]	Redshift	
	$log_{10}M_{\star}/M_{\odot}$	$\log_{10} \in [4, 12]$	Logarithm of formed stellar mass	
	$A_{V}$	$\log_{10} \in [-3, \ 0.7]$	V-band dust attenuation (AB mag)	
	$Z_{\star}$	$\log_{10} \in [-4, -1.3]$	Stellar metallicity where $\log_{10} Z_{\odot} = -1.7$	
	sSFR	$\log_{10} \in [-12, -7]$	Specific star formation rate (yr <sup>-1</sup> )	
	t <sub>25/50/75</sub>	Uniform $\in [0, 1]$	Normalized fraction of lookback time at which $25/50/75\%$ of the total mass had formed.	
	$\log U$	-2	Ionization parameter	
	$f_{ m esc}$	0.0	Ionizing photon escape fraction	
	$f_{ m esc,\; Ly}{}_{lpha}$	0.1	Escape fraction of Lyman- $\alpha$ photons	
	n	-0.7	Power-law slope of Calzetti et al. (2000) attenuation	
	$T_{dust}$	40 K	Dust Temperature (Greybody)	
	β	1.5	Dust Emissivity (Greybody)	
	$\alpha$	1	Dirichlet concentration parameter for GP-SFH models	

# 4 TRAINING SBI MODELS

This section details the process of training our SBI model, Model 1, to infer galaxy physical parameters (e.g., stellar mass, SFH, dust attenuation) from broadband photometric observations. The process involves two main stages: first, constructing the input data arrays, and second, optimizing the neural network architecture and training procedure.

# 4.1 Feature Engineering

Starting with the comprehensive library of simulated photometry generated in the previous section, we perform several feature engineering steps to construct the final parameter  $(\theta)$  and observation (x) arrays for training. This process is crucial for tailoring the general simulation library to a specific application and for ensuring the numerical stability of the training process. Key steps include selecting the specific photometric filters or wavelength range and resolution that match our observational dataset, transforming the data to a more suitable unit system and optionally applying a realistic noise model to the simulated fluxes. We also include measurements of photometric uncertainty in each filter as part of the observation array for each sample to allow the model to condition posterior estimates on the known uncertainty in the photometry.

For the application in this paper, we select the 14 photometric filters from HST/ACS and JWST/NIRCam that provide coverage over the full GOODS-South field, as detailed in Section 5.1. We then apply a custom, empirically derived noise model to the simulated fluxes to match the noise characteristics of the JADES survey data, a process we describe in Section 4.2.

For numerical stability and to handle non-detections gracefully, we convert all photometric fluxes into *asinh* magnitudes (Lupton et al. 2004), which have useful properties for inference. This unit system behaves logarithmically for bright sources but is linear for faint sources, avoiding issues with negative or zero fluxes. For a flux *f* the scaling to an *asinh* magnitude *m* is as follows

$$m = -2.5 \log_{10}(e) \left[ \operatorname{asinh} \left( \frac{f}{2f_b} \right) + \ln \left( \frac{f_b}{3631 \text{ Jy}} \right) \right]$$
 (4)

where  $f_b$  is a softening parameter, which we set to the filter-dependent  $5\sigma$  flux limit of our observational data. The corresponding magnitude error is

$$\delta m = \frac{2.5 \log_{10}(e) \times f}{\sqrt{f^2 + (2f_b)^2}} \tag{5}$$

We set the scaling parameter  $f_b$  to the  $5\sigma$  detection level for each filter, which we discuss further in Section 4.2. The relationship between the AB and *asinh* magnitudes, and the role of the softening parameter  $f_b$  is illustrated in the upper panel of Figure 2.

The final input observation vector for our fiducial model, Model 1, consists of 29 features: the *asinh* magnitude and its associated error in each of the 14 filters, plus the galaxy's redshift, which we treat as a known quantity. The target parameter vector consists of 11 parameters. This includes the 7 primary parameters which fully parametrize the model; stellar mass ( $\log_{10} M_{\star}$ ), metallicity ( $\log_{10} Z_{\star}$ ), dust attenuation (A<sub>V</sub>), four SFH parameters (SFR, t<sub>25</sub>, t<sub>50</sub>, t<sub>75</sub>, but also four derived parameters: SFR averaged over 10 Myr (SFR<sub>10</sub>), surviving stellar mass ( $\log_{10} M_{\star}^{\rm surv}$ ), mass-weighted age ( $t_{M_{\star}}$ ), and UV slope ( $\beta$ ). SBI lets us directly infer these derived parameters alongside the primary parameters which control our model. We use the same broad, uninformative priors for training the SBI model as were used to generate the initial simulations (see Table 2.) For the derived parameters we simply use broad uniform priors between the minimum and maximum values present in the training dataset.

#### 4.2 Noise Modelling

The output of our SYNTHESIZER SED modelling is noiseless photometric fluxes we will call x. For a full-forward model which matches our observed data  $x_{\rm obs}$ , we need a process to construct x', noisy photometry which reproduces the noise characteristics of  $x_{\rm obs}$ .

The simplest approach, treating each filter as independent and given a measurement of the average depth in each filter  $\sigma_f$ , would be to say  $x_f' = \mathcal{N}(x_f, \sigma_f)$  for each filter f, where  $\mathcal{N}$  is the Normal distribution. This is an approximation, as in reality  $\sigma_f$  will be dependent on  $x_f$ , and is likely to vary across the survey. It will also in some cases correlate with the depth in other filters, e.g. in surveys

with a central deep region plus peripheral shallower imaging, e.g. the Hubble Ultra Deep Field (HUDF).

If the model is provided the photometric uncertainty estimate, in order to condition the posteriors to account for photometric noise, then we note that strictly this would not be  $\sigma_f$ , but rather  $\sigma_f'$ , the prediction of the uncertainty given the scattered flux x'. For real observations we can not know the true kernel which scattered the photometry, and must estimate the uncertainty dependent on the noisy observation.

For Model 1, we construct our per-filter noise modelling to match the noise properties of the observational dataset we introduce in Section 5.1. Given the per-band flux and local flux uncertainty estimates produced by the GALFIND catalogue creation (outlined in Section 5.1) process for all sources in the catalogue, we first calculate the median  $5\sigma$  depth, which we use for the *asinh* magnitude parameter  $f_b$ . Then we convert flux and flux error to *asinh* magnitudes following Equation 4 and Equation 5, and bin them into 20 uniformly distributed magnitude bins. For each bin we compute the median and standard deviation in the magnitude error, which we use to define two linear interpolators  $f_m$  and  $f_{\sigma}$  to predict  $x_m$  and  $\sigma_m$  given an input *asinh* magnitude m.

For an input magnitude m the process to generate the scattered magnitude and magnitude error is as follows:

- (i) Predict  $x_m = f_m(m)$  and  $\sigma_m = f_{\sigma}(m)$  given m
- (ii) Draw noise kernel  $\phi = \mathcal{N}(x_m, \sigma_m)_{[0,\infty]}$
- (iii) Draw noisy magnitude  $m' = \mathcal{N}(m, \phi)$
- (iv) Predict magnitude error  $\sigma' = f_{\sigma}(m')$

This process realistically reproduces the noise properties of the observational data, as illustrated for the F444W filter in Figure 2, which shows the median and  $1/2\sigma$  regime of our noise model relative to a random sampling of the true photometric uncertainties drawn from the JADES photometric catalogue.

# 4.3 Model Architecture and Hyperparameters

We use LTU-ILI as the backend for training our SBI model, which provides a unified interface to established libraries such as sbi (Tejero-Cantero et al. 2020) and LAMPE<sup>2</sup>. As listed in Table 3, a variety of neural network architectures are supported by these backends, but for Model 1 we test two density estimators: the flexible *neural spline flow* (NSF, Durkan et al. 2019) and the *mixture density network* (MDN, Bishop 1994).

These density estimators can be sensitive to the hyper-parameters controlling the depth and width of the neural network. For a NSF this is parametrized as hidden\_features and num\_transforms, where the number of hidden features control the width of the hidden layers in the neural networks which make up the spline transformations and the number of transforms controls the number of invertible transforms composed into the flow.

To find the optimal configuration for our problem, we use the Optuna framework (Akiba et al. 2019) in order to determine the best hyperparameters for our model. We performed approximately 3000 parallel trials, exploring the parameter space listed in Table 3. Each trial utilized the Model 1 realization with 10<sup>5</sup> samples for computational efficiency and we used Optuna's MedianPruner to terminate unpromising trials early, thereby accelerating the search. The objective was to maximize the validation log-probability.

The results of this optimization are shown in Figure 3. The upper

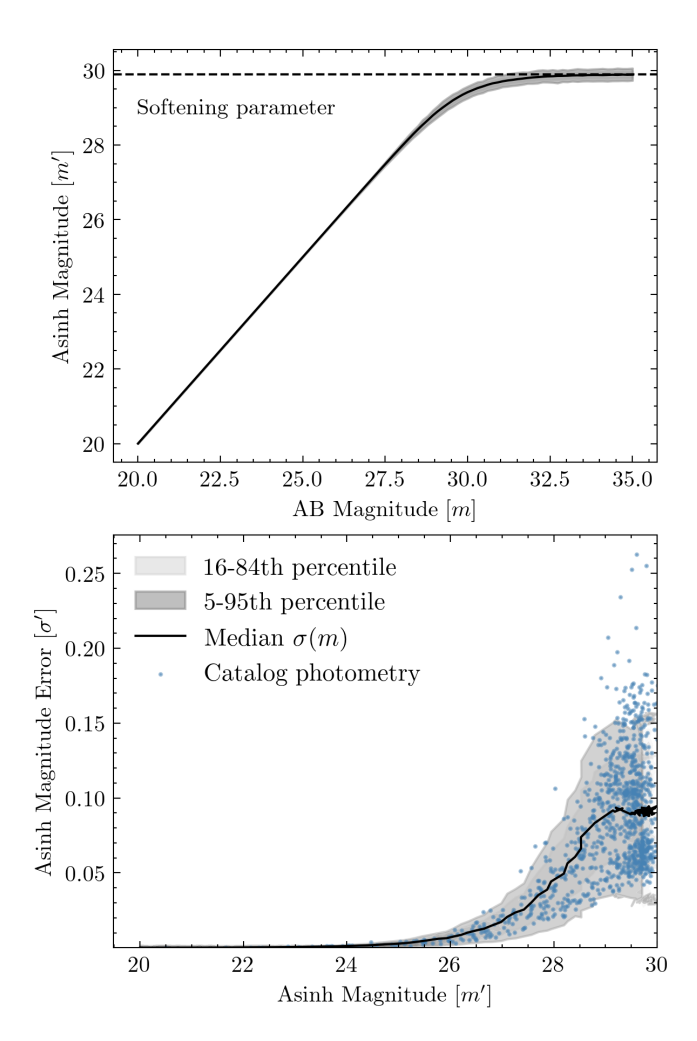


**Figure 2.** An illustration of the empirical noise model for the F444W filter. The upper panel shows the relationship between the noiseless input magnitude (m) and the scattered, noisy magnitude (m'). The lower panel shows the relationship between the input magnitude and the assigned photometric uncertainty  $(\sigma')$ . The blue points show true flux and uncertainty measurements from the JADES photometric catalogue.

panel shows parameter importance for both the full set of trials and for the NSF and MDN network architectures alone. The NSF architecture was consistently preferred over the MDN in our trials, achieving higher log-probabilities. The lower panel shows log probability contours for a subset of the optimization parameters; the learning rate, training batch size, early stopping criteria, and the number of hidden features and transforms/components for the NSF and MDN.

The optimization metric had a significant dependence on several hyper-parameters, in particular the number of transforms, the learning rate and training batch size. The optimal trial utilized a NSF with 30 hidden features and 14 transforms, trained with a Kingma & Ba (2014) optimizer, with a training batch size of 79 and a learning rate of 7e-4. Trials with higher numbers of transforms perform more poorly, which may be because the model over-fits to the training dataset, due to the higher number of free parameters in the flow. The best learning rate, which controls the optimizer step size, is well-constrained, with learning rates which are too large or too small jumping over minima or getting stuck in local minima, respectively. Further improvements to the model may be made by utilizing a learning rate scheduler, which decreases the learning rate as the model approaches a minima. The early stopping criteria, which controls the

https://github.com/probabilists/lampe

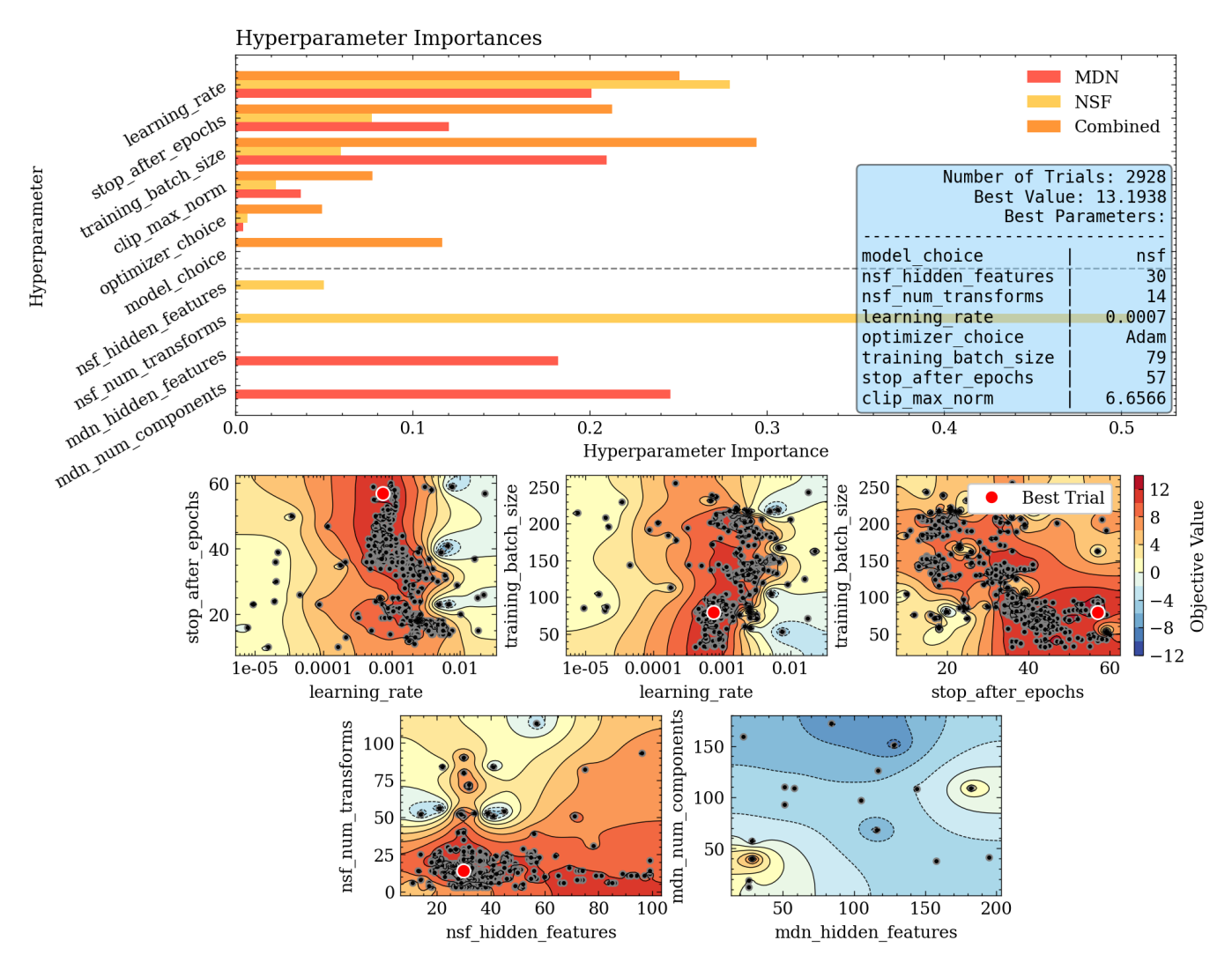


Figure 3. Model 1 NPE hyperparameter importance and logarithmic  $P(\theta|x)$  contours for key hyperparameters as determined by Optuna testing (Akiba et al. 2019). The upper panel shows the importance of each hyperparameter to the objective optimization for the overall trial, as well as individually for the mixture density network (MDN) and neural spline flow (NSF) network architectures we tested. The lower panels show objective contours for hyperparameter pairs for the learning rate, training batch size, early stopping criteria and network specific parameters controlling the width and depth of the neural networks. Based on  $\sim$ 3000 trials, the optimal model utilized a NSF architecture with hyperparameters given in the inset table.

number of epochs without improvements which are trained before training is stopped, is approaching the prior bound, but good results are obtained anywhere from 30 epochs and up, which provide a good compromise between allowing the model to condition well to the data without over-fitting.

# 4.4 Model Training and Validation

Our final model realization used the optimized hyper-parameters, but trained on a larger model grid of  $N=10^6$  observations. This model took  $\sim 3$  days to train on a desktop CPU (distributed across 20 cores). 10% of the training dataset was withheld for use during model validation. Model validation consists of testing the accuracy and bias of the model, as discussed in Section 2.3.3. Model coverage tests such as SBC and TARP are implemented in L<sub>T</sub>U-ILI and are run automatically by SYNFERENCE.

As this example model was trained with a noise model matched to observational data from JADES, there are regions of the parameter space (e.g. low mass galaxies at high redshift) where we cannot expect

accurate parameter recovery as the noise level dominates over the mock photometry. However an unbiased SBI model should still return the unconstrained prior proposal in the noise-dominated case. When evaluating parameter recovery we limit ourselves to observations within the validation set which have an average signal to noise in the long-wavelength NIRCam wideband filters SNR > 5, but we utilize the full test dataset for the TARP and SBC metrics.

For each parameter we compute the Root Mean Square Error (RMSE) and the co-efficient of determination  $R^2$ :

RMSE = 
$$\sqrt{\frac{1}{n} \sum_{i=1}^{n} (x_i - \hat{x}_i)^2}$$

which quantifies the deviation between the true and recovered parameter value.  $R^2$  is given by

$$R^{2} = 1 - \frac{\sum_{i=1}^{n} (x_{i} - \hat{x}_{i})^{2}}{\sum_{i=1}^{n} (x_{i} - \bar{x})^{2}}$$

Table 3. An overview of the relevant model architectures available in LTU-ILI, and the hyperparameter ranges and optimal values used in our Optuna optimization.

#### **Backends and Network Architectures**

sBI: Mixture density network (MDN, Bishop 1994); Masked autoregressive flow (MAF, Papamakarios et al. 2018);

Neural spline flow (NSF, Durkan et al. 2019): Masked Autoencoder for Distribution Estimation

(MADE, Germain et al. 2015) LAMPE: MDN: MAF: NSF:

Continuous normalizing flow (CNF, Chen et al. 2018; Grathwohl et al. 2018)

Hyperparameters

11yper par ameters								
Range	Optimal Value							
$NSF \lor MDN$	NSF							
Adam ∨ AdamW	Adam							
$[5 \times 10^{-2} - 10^{-6}]$	0.0007							
[3 - 20]	14							
[10 - 100]	30							
[10 - 200]	-							
[10 - 600]	-							
[32 - 256]	79							
[10 - 60]	57							
[0.1 - 10]	6.66							
	Value							
-	10%							
-	10%							
	Range NSF ∨ MDN Adam ∨ AdamW [5 × 10 <sup>-2</sup> - 10 <sup>-6</sup> ] [3 - 20] [10 - 100] [10 - 200] [10 - 600] [32 - 256] [10 - 60]							

which measures the proportion of the variance in the dependent variable that is predictable from the independent variable, with a value closer to 1 showing a more reliable prediction. In these equations: n is the total number of validation samples.  $x_i$  is the i-th true value,  $\hat{x_i}$  is the i-th predicted value, and  $\bar{x}$  is the mean of all the true values  $x_i$ .

These results are shown in Figure 4. The upper panels show the parameter recovery for a subset of the fitted model parameters, including the total and surviving stellar masses, the star formation rate, dust attenuation, mass-weighted age and UV  $\beta$  slope (between 1250Å and 3000Å). We plot density hexbins showing the true and recovered values for the full posterior estimates for each parameter. We find generally good parameter recovery for these parameters, with high values for the coefficient of determination  $R^2$  suggesting high correlation between true and recovered parameter estimates. Inset into each panel are the rank histograms, which evaluates model calibration by plotting the distribution of the true value's rank relative to sorted samples from the model's posterior predictive distribution; a flat, uniform histogram is ideal, indicating that the true values are statistically indistinguishable from the predicted sample, whereas a histogram which is more bell-shaped means that the learned posterior is too wide. The rank histograms shown are generally flat or slightly bell-shaped indicating that the posterior distributions in Model 1 could be tighter than is produced by the model.

The individual SFH parameters are more difficult to recover due to significant degeneracy between parameters. In particular with the GP-SFH model, the disconnect between the recent SFR and the historic SFH represented by the  $t_{25/50/75}$  parameters means that disparate combinations of these parameters can produce functionally similar star formation histories. To combat this we also infer SFH proxies, such as the 10 Myr averaged SFR and the mass-weighted age, which can break this degeneracy, and show significantly better parameter recovery.

The lower panels of Figure 4 showing the overall model 'TARP' metric and individual coverage plots for parameters suggests the model is unbiased and produces accurate posterior estimates, as both metrics closely follow the 1:1 line for all parameters. The coverage plots evaluate the nominal credible level (the "expected" coverage

Table 4. Model performance metrics for each parameter, including the coefficient of determination  $(R^2)$  and Root Mean Square Error (RMSE). The  $R^2$  values are calculated across the full validation dataset. The RMSE is also calculated for high-signal-to-noise (SNR) subsets of the validation set (SNR≥ 5 and SNR≥ 20, as measured in F277W, F356W and F444W). This high-SNR case tests the model's underlying accuracy for parameter recovery, independent of uncertainties from photometric scatter (noise).

Parameter	$\mathbb{R}^2$	$\sqrt{ \sigma^2 }$	$\sqrt{ \sigma^2_{>5\sigma} }$	$\sqrt{ \sigma_{>20\sigma}^2 }$
$\log_{10} \mathrm{M_{\star}/M_{\odot}}$	0.99	0.75	0.21	0.18
$\log_{10} Z_{\star}$	0.96	0.72	0.43	0.37
$\log_{10} A_{V}$	0.86	0.94	0.64	0.61
log <sub>10</sub> SFR	0.88	1.28	0.64	0.57
$t_{25}$	0.95	0.19	0.19	0.19
$t_{50}$	0.88	0.20	0.20	0.21
$t_{75}$	0.77	0.19	0.20	0.17
$\log_{10} t_{mwa}$	0.98	0.20	0.17	0.17
log <sub>10</sub> SFR <sub>10Myr</sub>	0.90	1.15	0.55	0.48
$\log_{10} M_{\star,surv}/M_{\odot}$	0.99	0.73	0.20	0.63
β	0.86	1.02	0.25	0.20

probability, e.g., 95%) on the x-axis against the empirical coverage (the actual proportion of true values that fall within that predicted interval) on the y-axis. Perfect calibration is represented by the 1:1 diagonal line represents where the model's reported uncertainty (e.g., a 95% interval) perfectly matches its empirical performance. Model 1 shows well-calibrated posteriors for all parameters.

We also evaluate a range of model benchmarks to evaluate the overall model performance as well as per-parameter metrics, which we show in Table 4. These include the coefficient of determination  $R^2$  and the root mean square error.

# 4.4.1 Comparison to Nested Sampling

To obtain reference posterior estimates for observations within our validation dataset we use Bayesian nested sampling implemented through the DYNESTY package. DYNESTY provides Bayesian posterior and evidence estimates. We run the dynamic nested sampling algorithm in DYNESTY using slice sampling to propose new points, implementing multi-ellipsoidal bounding for efficiency. The process starts with 250 live points, and the initial run continues until the estimated improvement in evidence ( $\Delta log Z$ ) drops below 0.1.

We use  $\mathcal{L} = -\frac{1}{2}\chi^2$  as our likelihood function, and use the same SYNTHESIZER based model to generate mock photometry for each likelihood evaluation. DYNESTY takes ~90 minutes per fit on a single CPU core, which is computationally prohibitive for the full validation set, so we have chosen a selection of observation vectors from the validation set which cover significantly different regions of the parameter space.

In Figure 5 we show a corner plot showing the multivariate posterior distribution for a random example galaxy from the validation set for both Model 1 and the nested sampling results from DYNESTY. We also show the ground truth parameter values in black. We observe strong agreement between both the univariate and multivariate posterior distributions for all fitted parameters in this test case. Interestingly, both the Model 1 and NS results identify the same slightly bi-model result for metallicity, although they disagree slightly on it's relative probability. We recover the ground-truth values within  $1\sigma$ for all parameters.

We also show the reconstructed SED and SFH for the galaxy which we derive by calculating the predicted SED for each posterior draw, and taking the 16th/50th/84th percentiles of the distribution to find the median and  $1\sigma$  confidence interval for both the Model 1 and NS

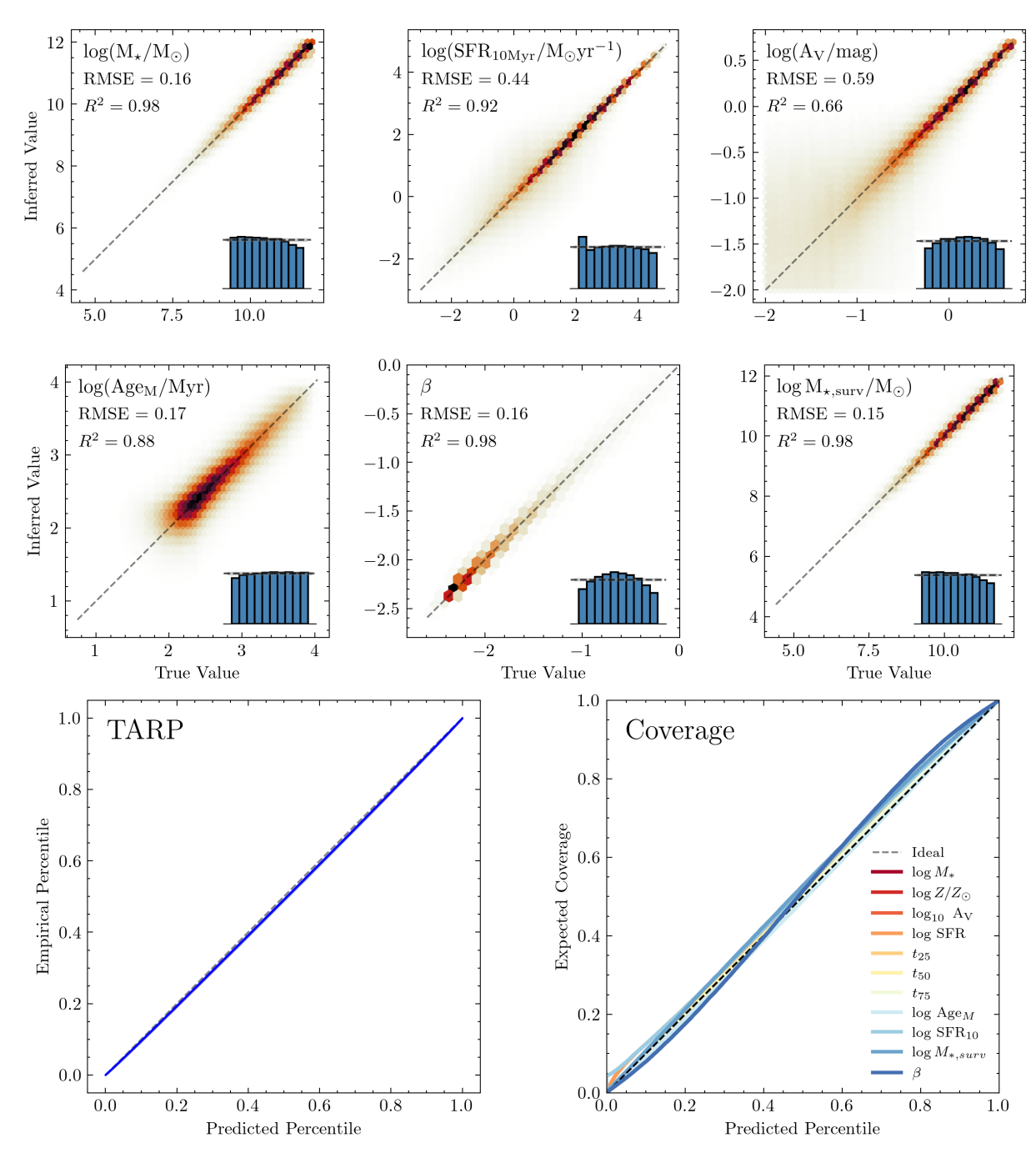


Figure 4. Model performance metrics and calibration tests for Model 1. Upper panels: True vs recovered parameter estimates for key model parameters as meausred with the subset of the validation dataset with  $\langle SNR \rangle > 5$ . Each panel has the posterior rank histogram inset showing the posterior calibration, and the coefficient of determination  $R^2$  and root mean square error (RMSE) are provided for each parameter. A rank histogram evaluates calibration by plotting the distribution of the true value's rank relative to sorted samples from the model's posterior predictive distribution; a flat, uniform histogram is ideal, indicating that the true values are statistically indistinguishable from the predicted samples. Lower right: Coverage plots for individual parameters showing unbiased estimates. This compares the nominal credible level (the "expected" coverage probability, e.g., 95%) on the x-axis against the empirical coverage (the actual proportion of true values that fall within that predicted interval) on the y-axis. The 1:1 diagonal line represents perfect calibration, where the model's reported uncertainty (e.g., a 95% interval) perfectly matches its empirical performance (it contains the true value exactly 95% of the time). Lower left: Tests of Accuracy with Random Points metric (TARP, Lemos et al. 2023) showing the model calibration relative to the ideal 1:1 line. TARP evaluates the average calibration of the model across the entire data distribution. It plots the nominal credible level (x-axis) against the expected coverage probability (y-axis), which is the empirical coverage averaged over all possible data points.

posterior estimates. The reconstructed SEDs and SFHs both closely reproduce the ground-truth model, and the reconstructed photometry also recovers the input photometry used for the inference, which shows the model has accurately learnt the observation-parameter relationship in this case.

#### 4.5 SED Recovery

We show the true and recovered SEDs and ACS\_WFC/NIRCam photometry for a range of input galaxy parameters in Figure 6, which reflect the observed diversity of galaxies. We include galaxies from the local Universe to high-redshift, with SFHs ranging from quiescent to a starburst, and from entirely dust-free to very obscured. The shaded volume for each galaxy show the range of SEDs consistent with the posterior draws for that input photometry, which we compare with the true input SED in dark blue.

For all eight distinct galaxy models shown the SBI posterior estimates produce SEDs which are close to the true underling galaxy SED, suggesting the model has learnt the observation-parameter relationship across a wide range of input parameters reflecting highly diverse physical galaxy properties.

# 5 APPLICATION TO OBSERVATIONS

The purpose of training our SBI model is to perform inference on real observations, where we have no knowledge of the ground truth. Our chosen dataset is a photometric catalogue of galaxies within the GOODS-South field, which is a well-studied region with a large amount of ancillary observations including space and ground-based spectroscopic redshifts.

#### 5.1 Data Products and Catalogue

In this section we detail the photometric and spectroscopic data products used to construct our galaxy catalogue upon which we validate our SBI model.

# 5.1.1 Photometric Data Products

We use the JWST NIRCam imaging of the GOODS-South field taken as part of the JWST Advanced Deep Extragalactic Survey (JADES; Eisenstein et al. 2023b, see also Bunker et al. (2023) and Hainline et al. (2024)). This includes the F090W, F115W, F150W, F200W, F277W, F335M, F356W, F410M, and F444W NIRCam data presented in Rieke et al. 2023b (DR1) and additional area from PIDs 1180 (PI: D. Eisenstein), 1286 (PI: Lützgendorf), and 1287 (PI: Isaak). HST ACS legacy data for the F435W, F606W, F775W, F814W, and F850LP filters is taken from v2.5 of the Hubble Legacy Fields (Illingworth et al. 2016; Whitaker et al. 2019), for a total of 14 photometric filters.

# 5.1.2 Catalogue Creation

Our photometric reduction and catalogue creation process uses the GALFIND pipeline<sup>3</sup>, which has been previously used in the EPOCHS paper series (see. e.g. Adams et al. 2024; Conselice et al. 2025; Austin et al. 2024; Harvey et al. 2025b). For full details of the data reduction

and catalogue creation process for this field please see Austin et al. (in prep.).

In summary, we use a modified version of the official JWST pipeline, with CDRS version 1263, and align the image mosaics to Gaia DR3. For our catalogue creation we use SExtractor, and perform detection in an inverse-variance weighted stack of F277W, F356W and F444W. We measure aperture photometry in 0.23 diameter apertures as well as total photometry in elliptical Kron apertures.

Whilst the typical EPOCHS catalogue creation procedure is optimized for the study of high-redshift galaxies, we wish to validate our SBI methodology over a wider sample of galaxies. Therefore in a deviation from the standard EPOCHS approach we also measure total fluxes for each galaxy in a similar fashion to Weibel et al. (2024) and Weaver et al. (2024). We derive a correction factor from the flux ratio between the 0".32 aperture and the Kron aperture in a PSFmatched version of the detection image. In the case that the Kron aperture covers a larger area, and the measured ratio is greater than unity, we correct measured fluxes in all bands by this ratio before any aperture corrections are applied. We then calculate an aperture dependent PSF-correction for each galaxy by placing either the Kron or circular aperture on our F444W PSF model and measuring the enclosed flux. In the case that the Kron aperture extends beyond the  $4'' \times 4''$  extent of our PSF models, we approximate the Kron ellipse as a circle with radius KRON\_RADIUS  $\times \sqrt{A\_IMAGE} \times B\_IMAGE$ , and calculate the aperture correction from tabulated enclosed energy tables for NIRCam. This procedure results in flux measurements which account for the total light emitted by each galaxy, but without any distortion of the galaxy colour due to changing Kron apertures in different filters. Our PSF models are created by stacking isolated stars in each mosaic and follow the exact procedures of Harvey et al. (2025a).

# 5.2 Spectroscopic Data Products

We obtain spectroscopic redshift catalogues from previous studies using both space and ground-based spectroscopy, including JWST/NIRSpec (Jakobsen et al. 2022), 3D-HST, MUSE, and numerous smaller surveys including VLT/FORS2 amd VIMOS/VLT (Brammer et al. 2012; Bacon et al. 2010). For NIRSpec observations of the GOODS-South field we use the official JADES DR3 catalogue (D'Eugenio et al. 2025). We filter the catalogue by the spectroscopic redshift and its associated quality by:

$$(\texttt{z\_Spec\_Flag} = A \lor B \lor C) \land (\texttt{z\_Spec} > 0) \;,$$

which results in 1333 galaxies with robust spectroscopic redshifts from JWST/NIRSpec.

For 3DHST we use the v4.1.5 catalogues for both the HST imaging and grism observations (Brammer et al. 2012; Skelton et al. 2014; Momcheva et al. 2016), which we filter for robust spectroscopic redshifts following

$$((z_{max\_grism} \neq -1) \land (use\_zgrism = True)) \lor (z_{spec\_1} \neq -1)$$
.

For MUSE we obtain the MUSE HUDF DR2 catalogue (Bacon et al. 2023). We also obtain the ESO Master Catalogue v3.0, which compiles spectroscopic redshifts from surveys including Le Fèvre et al. (2004); Vanzella et al. (2005, 2006, 2008, 2009); Kurk et al. (2013), which target galaxies with I < 24. We filter the ESO catalogue for robust spectroscopic redshifts based on the quality factor column.

We perform a hierarchical matching to our master photometric catalogue, by matching each spectroscopic survey to a subset of the catalogue containing only galaxies with photometry (as determined

https://galfind.readthedocs.io

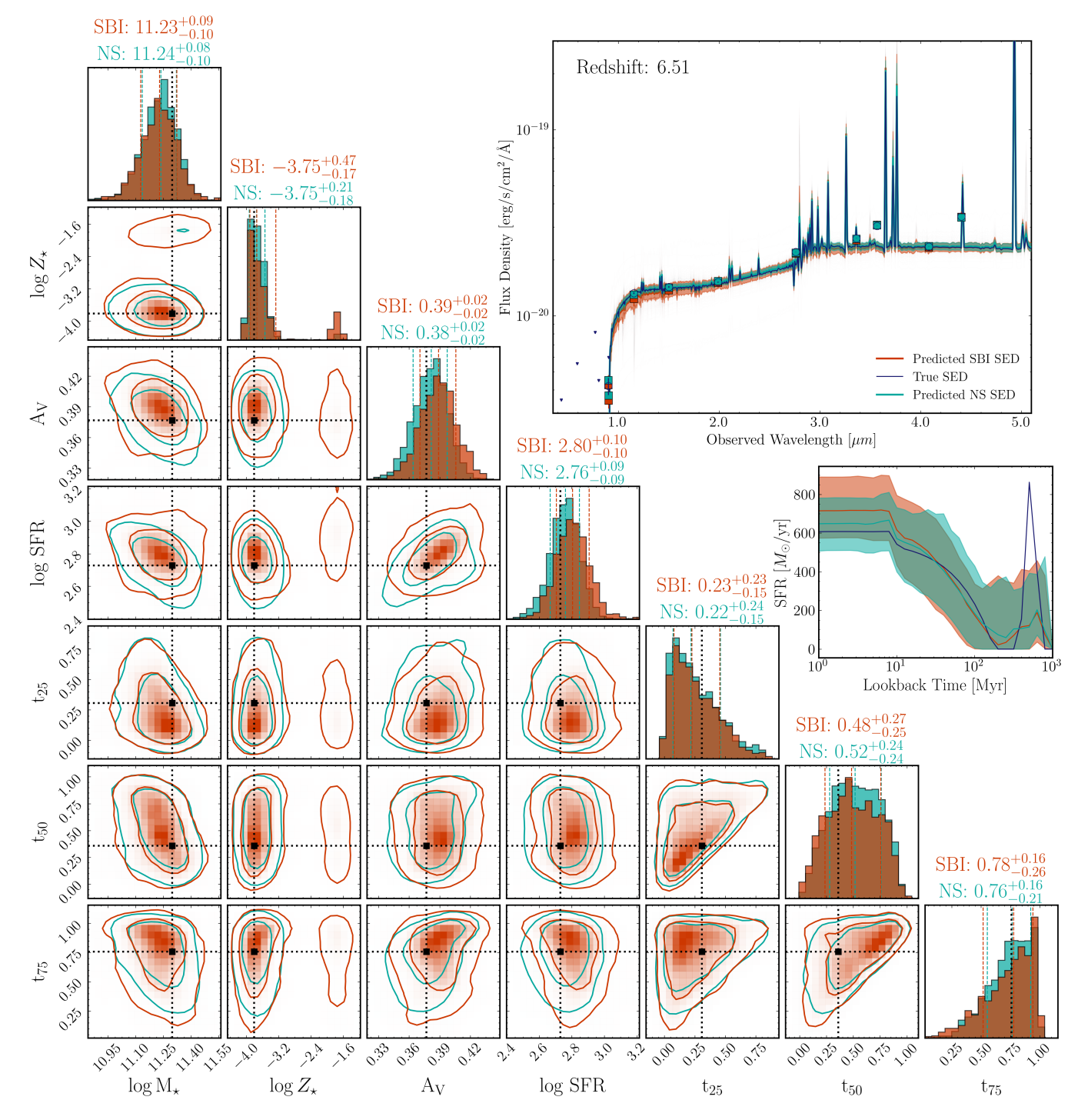


Figure 5. Corner plot for a single mock galaxy comparing multivariate posterior constraints from SBI (in red) to the ground-truth value (black point) as well as reference nested-sampling (labelled as NS) results using DYNESTY (in blue). Contours show the  $1\sigma$  and  $2\sigma$  regions. Model 1 accurately recovers the stellar mass, metallicity, dust attenuation and SFH. In the upper right the true and recovered SED and SFH models are shown showing accurate SFH and SED recovery for this galaxy in both cases.

by the flux in the nearest NIRCam filter to the approximate spectroscopic wavelength probed) bright enough to be detected given the sensitivity of the spectroscopic survey. If a galaxy is matched in multiple spectroscopic surveys we prioritize NIRSpec>MUSE>3D-HST>ESO, and keep only the highest priority spectorscopic redshift available to avoid source duplication. We allow a 0."5 offset for

MUSE, 3DHST and NIRSpec, and a 1".0 offset for the ESO catalog. We note however that the average offset is only 0".23.

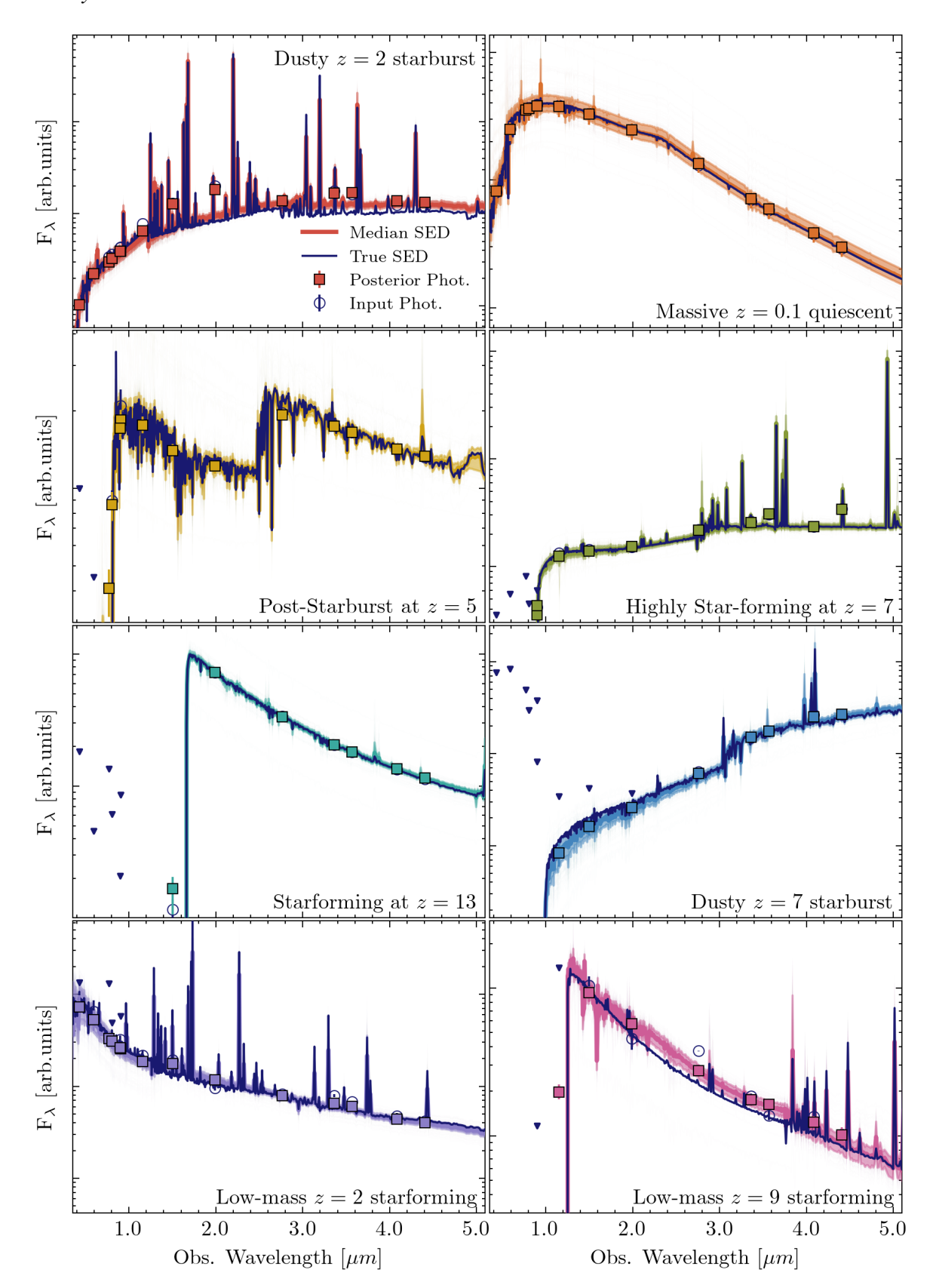


Figure 6. SED recovery with SBI inferred posterior parameters compared to true SED and photometry for 8 distinct regions of model parameter volume. Dark blue lines show the input spectra, and colored lines and shaded regions show the 50th and 16-84th percentile of the reconstructed SED using the posterior samples from Model 1. Photometry provided to the model for inference is shown with unfilled circles and downwards triangles, which correspond to measurements with SNR<3 and are plotted as a  $3\sigma$  upper limit for visual clarity given the logarithmic y-axis scaling. The model is able to successfully reproduce the input SEDs across different regions of the parameter hypervolume.

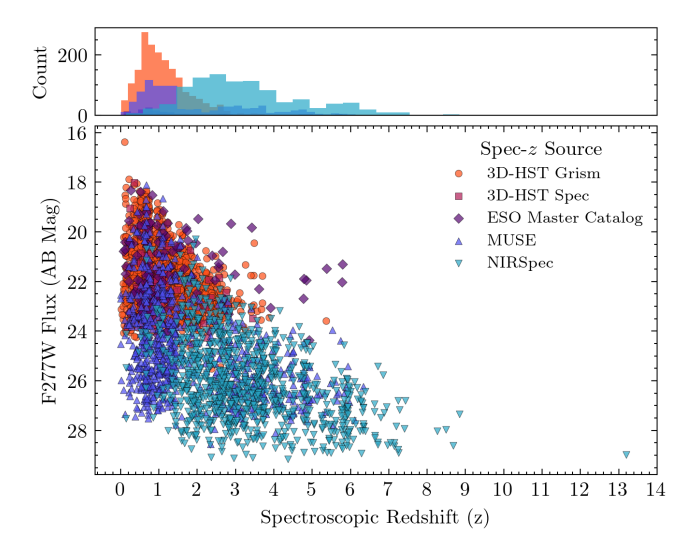


Figure 7. Apparent magnitude in the F277W filter vs redshift for our sample of  $\sim$ 3000 spectroscopically confirmed galaxies in the JADES GOODS-South field. Galaxies are split by the instrument used to determine their spectroscopic redshift, as detailed in Section 5.2. The upper panel shows a histogram of the spectroscopic sample as a function of redshift.

# 5.3 Final Catalogue

Our final spectroscopically-matched catalogue contains 3800 galaxies. We present a magnitude-redshift comparison to demonstrate our sample in Figure 7, which includes galaxies from 0 < z < 13.5.

SBI approaches do not work well with missing data, so for our basic catalogue we require robust flux measurements in the F606W, F775W, F814W, F850LP, F090W, F115W, F150W, F200W, F277W, F335M, F356W, F410M and F444W filters. Approaches in the literature such as Wang et al. (2023c) to infer missing observations through Monte Carlo approaches on the training dataset are computationally intensive. This cuts our catalogue down to 3,088 galaxies which have measured photometry in all required filters.

# 5.4 Testing model misspecification

A reasonable check before using any model to perform inference on an observation is that the model is capable of producing mock observations which are similar to the observation itself. This is referred to as "prior predictive checking" (Gelman 2006). This is particularly important when using an SBI approach, which requires the training data closely matches the observations. In SBI terminology if the model can't reproduce the observations, the model is 'mis-specified' to the data, and any inference from the model will be unreliable.

We carry out prior predictive checking using outlier detection, where we treat our training dataset as a reference distribution against which we test our observations to see whether they are identified as outliers. There are a large number of different approaches to outlier detection, which are suited to different problems. Our outlier detection utilizes majority voting of a suite of different outlier detection algorithms, such that for each observation  $\geq 50\%$  of the methods must identify the observation as an outlier.

In SYNFERNCE, prior predictive checks are carried out by default before inference to improve posterior reliability. This is implemented through the PYOD Python package (Zhao et al. 2019). We utilize a suite of 8 different outlier detection algorithms, including Isolation Forest (Liu et al. 2008; Tony et al. 2012), Local Outlier Factor (He et al. 2003), Deep Isolation Forest (Xu et al. 2023), Feature Bag-

ging (Lazarevic & Kumar 2005), ECOD (Li et al. 2022), k-Nearest Neighbors (Angiulli & Pizzuti 2002), Gaussian Mixture Modelling (Aggarwal et al. 2015), and Kernel Density Estimation (Latecki et al. 2007). Combining different outlier detection approaches averages over the individual biases of each method, and provides a more robust assessment than relying on a single method alone.

We set the outlier contamination at 1% for all outlier models in the ensemble. Only 0.25% of our GOODS-South catalogue is identified as a possible outlier by this approach, suggesting our training dataset covers almost the full range of color and luminosity space of our observational catalogue. The galaxies identified as outliers are not a homogenous population, with a wide range in redshift, stellar mass, SFR and  $A_V$ , based on the BAGPIPES results. Around 50% have  $A_{\scriptscriptstyle V}>1$  with BAGPIPES, so they may be being identified as outliers simply due to our logarithmic dust prior, which favours low dust attenuation.

## 5.5 Galaxy Property Inference

We apply our trained amortized NPE model to the photometric catalog to infer parameter posterior estimates. SYNFERENCE automatically applies the same model scaling and unit conversion to the observations as were applied to the training dataset, which is important for reliable results with SBI. We infer posterior distributions for our spectroscopic catalogue using Model 1, which takes 3 minutes for 3000 galaxies on a typical desktop CPU on a single core (17.5 galaxies/second), which could be further improved when the inference is distributed across multiple threads.

As a point of comparison we also fit the full galaxy sample with BAGPIPES, sampling using MULTINEST (Feroz et al. 2009). We use a modified version of BAGPIPES which can implement the same underlying SPS grid, priors and SFH model as Model 1 in order to obtain as representative a comparison as possible. The total time for this inference with BAGPIPES is  $\sim\!80$  CPU-hours, which is  $1700\times$  slower than the SBI model. We estimate parameter values and  $1\sigma$  uncertainties from the 16/50/84th percentiles of the posterior distributions for each parameter.

Figure 8 shows a comparison of the recovered stellar mass, star formation rate, dust attenuation and mass-weighted age between the BAGPIPES and Model 1 results. The stellar mass comparison for both models is the surviving stellar mass, which excludes stellar remnants and mass loss. These plots show the majority of the galaxies within the density contours, and only galaxies <20% of the peak density are shown with individual points and errorbars. We also show a rolling median in blue highlighting the overall trend.

In the upper left-hand panel the stellar mass estimates with Model 1 and BAGPIPES show excellent agreement, with a median offset of 0.03 dex. There are a few extreme outliers, which are primarily galaxies with both high-mass quiescent (with strong Balmer breaks) and low-mass (highly star-forming) solutions, on which BAGPIPES and SYNFERENCE disagree.

The SFR estimates also show reasonable agreements in most cases, but have more systematic offsets particularly at very low star-formation rates, where synference is finding systematically higher star-formation rates. The overall median offset is 0.086 dex. This in part likely due to a slight prior difference between synference and bagpipes. For synference each galaxy has an individual flat sSFR prior of  $-12 \le \log \text{sSFR/yr} < -7$ , whereas this has to be set globally with bagpipes. This leads to a higher lower limit on sSFR for massive galaxies using synference, as there is little observational difference between different sSFR values within the quiescent regime.

The lower left panel shows the mass-weighted age comparison between SYNFERENCE and BAGPIPES which also shows reasonable

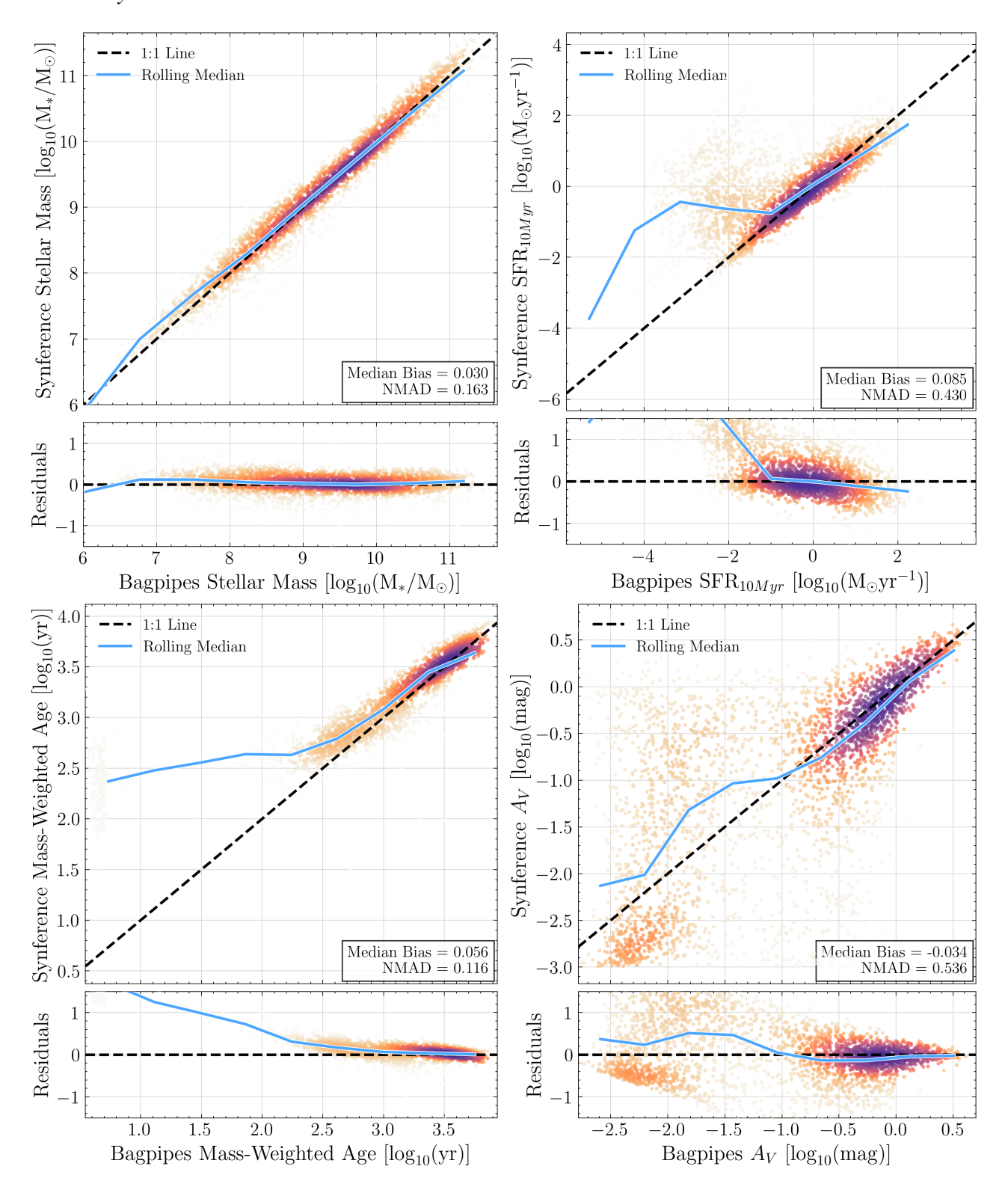


Figure 8. BAGPIPES VS. SYNFERENCE physical property inference comparison for the JADES spec-z catalogue, showing stellar mass (upper left), 10 Myr starformation rate (upper right), mass-weighted age (lower left) and dust attenuation (lower right). Points are colored by their local density as determined by a Gaussian KDE. The median offset (bias) and the NMAD (Normalized Median Absolute Deviation), a robust measure of the scatter, are inset into the panel for each parameter. Overall we find good agreement in recovered parameters with BAGPIPES, although there are some systematic deviations in certain regions of the parameter space. The inferred stellar mass shows little bias and relatively low scatter, whereas SFRs and stellar ages are typically systematically higher when using synference. Dust attenuation shows good agreement when there is significant dust present, but shows significant scatter for low dust attenuation, where the distribution skews towards the median of the prior. The deviation from the 1:1 line for low ages is due to BAGPIPES inferring a population of galaxies where all star-formation has occurred in a single burst immediately prior to observation, whilist SYNFERENCE prefers a slightly longer SFH.

agreement, particularly for higher stellar ages. The median offset is 0.057 dex. There are a group of outliers in the BAGPIPES results which are fitted with unphysical extremely young SFHs, where all mass formed in a very recent burst. These galaxies fall into the region of the Dense Basis SFH parameter space where the SFH is controlled only by the recent SFR parameter, rather than the lookback time quantiles. This may be causing an issue with the nested sampling causing the fitting to perform poorly and not find the optimal solution.

Finally for the dust attenuation,  $A_V$ , we also see good agreement, albeit with a wider scatter. For very low dust attenuation values we see a large amount of scatter, which is primarily due to the logarithmic scale, as there is very little difference observationally between  $A_V = 10^{-2}$  mag and  $A_V = 10^{-3}$ mag. The median offset is -0.033 dex.

Overall whilst there are some systematic differences between the BAGPIPES and SYNFERENCE results, they are no worse than other comparisons between different SED fitting codes, which often show different solutions when fitting the same galaxies (e.g. Harvey et al. 2025b).

# 6 DISCUSSION

In this section we briefly discuss the overall model performance, possible applications, limitations, and make comparisons with existing SED fitting tools.

#### 6.1 Posterior Accuracy

The performance metrics on the validation data, nested sampling comparison and BAGPIPES comparison show that the fiducial model performs well, and can accurately recover parameters such as stellar mass, star-formation rate, dust attenuation and stellar age to a reasonable accuracy. However, as demonstrated by the average RMSE at different SNR limits in Table 4, some parameters are still affected by significant scatter even at high SNR, which is independent of the error introduced by the photometric scatter. This is particularly true for parameters which are significantly degenerate with one another, such as the 4-parameter Dense Basis SFH. Whilst the recent SFR and overall age of the stellar population can be constrained when reconstructing the full SFH, Model 1 sometimes produces uncertain results for the overall SFH, where the lookback time quantiles  $(t_{25/50/75})$  posteriors are often prior-driven. We note that these degeneracies are not specific to this model but are implicit simply due to the information available from photometry alone. They are not induced by the neural density estimator, and are also observed in the nested sampling and BAGPIPES results (as can be seen in the reconstructed SFH in Figure 5, and would be observed in any SED fitting code when fitting the same observations.

# 6.2 Speed of Inference

Here we evaluate the speed of amortized inference with SBI compared to traditional Bayesian SED fitting as well as maximum likelihood modelling/optimization algorithms, i.e. for photometric redshifts with EAZY-py.

Figure 9 shows a comparison of the inference speed of our example models with SYNFERENCE compared to other commonly used SED fitting tools. For SYNFERENCE, which can utilize both the CPU and GPU for inference, we plot them separately. We note that GPUs do not typically offer a large speedup compared to CPUs for SBI models as the underlying neural networks within the NDE are relatively shallow.

GPU performance will provide the largest speed-up if an embedding network with convolutional components is utilized alongside the SBI model for e.g. dimensionality reduction.

This figure demonstrates one of the key strengths of the SBI approach, which is the speed of amortized inference. Depending on the neural network architecture we can perform inference at 20-100 galaxies/second per galaxy using synference, which is >3 orders of magnitude faster than with BAGPIPES or PROSPECTOR. Whilst neural network emulators like Parrot are also very powerful when used to speed up likelihood evaluations in SED fitting, utilizing them in this fashion is still significantly slower than direct NPE, which altogether bypasses likelihood evaluations entirely.

Purely as a demonstrative example Figure 9 shows the inference speed required to match the average speed at which galaxies are being observed across Euclid's 6 year mission, if processed in serial concurrently with detection (Euclid Collaboration et al. 2025). Whilst unrealistic, this is purely to demonstrate the volume of new galaxy observations which are currently being observed, and the scale of the data which will soon be available, if are able to make use of it.

The speed of inference of the SBI model can depend on the observational data used for inference, and can be reduced significantly if the model is misspecified relative to the observations, or is simply not well optimized in general. This is because in the SBI framework whilst we employ prior constraints on our parameter sampling space, these constraints are not explicitly known by the neural network density estimator, which can produce samples outside of the parameter bounds, which is known as 'leakage'. The prior constraints are instead utilized for accept-reject sampling when determining whether all parameter draws in a given posterior sample are within the prior bounds. How often a model produces samples outside the prior volume can significantly impact the sampling speed and cause low parameter acceptance. This problem is multiplied when sampling models with high dimensionality, as a rejected value for any dimension will reject the entire posterior sample. This can reduce the sampling speed for individual objects by several orders of magnitude relative to normal inference speed, and sometimes lead to the inference getting 'stuck', with low or essentially zero accepted samples. In synference this is handled by setting a maximum sampling time (10 - 30s) per galaxy, beyond which samples are instead sampled directly from the prior distribution.

# **6.3 Redshift Inference**

Spectroscopic redshifts are not typically available for the majority of galaxies in a photometric survey, especially in wide area photometric surveys (e.g. Euclid, LSST, Roman) where SBI techniques are particularly useful due to the speed of inference. In this case we can either rely on external photometric redshift estimates, e.g. template fitting with EAZY-py (Brammer et al. 2008) or ML-based photometric redshifts (Firth et al. 2003; Collister & Lahav 2004; Salvato et al. 2019; Newman & Gruen 2022), or we can treat the redshift as unknown during inference and directly infer the redshift posterior from the observations. We train a version of our model with the same training data and hyperparameters, where we do not provide the redshift as a feature but instead train the network to learn the redshift. We refer to this as Model 2.

In Figure 10 we show the spec-z vs. photo-z comparison for the spectroscopic galaxy sample. We find an outlier fraction ( $|\Delta z|/(1+z)>0.15$ ) of  $\eta=0.117$ , a normalized median absolute deviation (NMAD) of 0.055 and a bias of -0.043. The lower panel shows  $\Delta z/(1+z)$  as a function of the spectroscopic redshift. We observe that the primary outlier source is Lyman-Balmer break confusion, and that

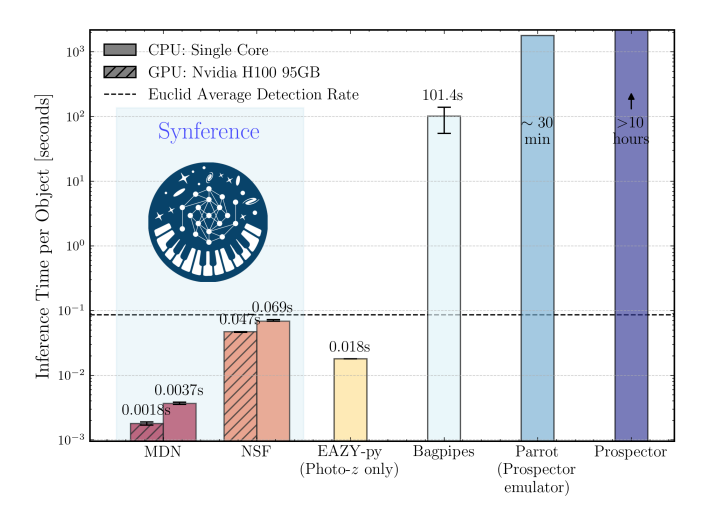
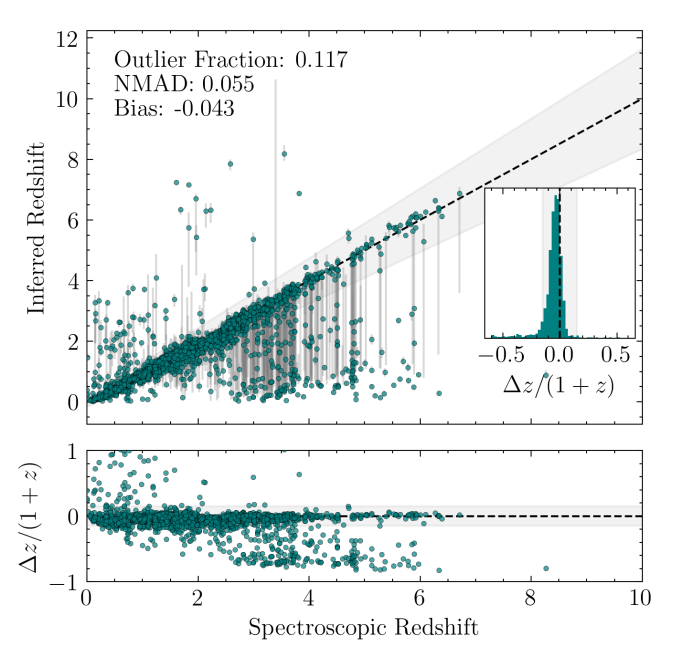


Figure 9. Comparison of inference speed with SYNFERENCE (using Model 1, and a MDN variant of Model 1) for different hardware and density estimator choices to other SED fitting tools such as EAZY-py, BAGPIPES and PROSPECTOR, run on the same galaxy sample. For CPU based inference we show single core performance to ensure a fair comparison. We also show the approximate speed of the Prospector emulator Parrot, from (Mathews et al. 2023; Wang et al. 2023a). The horizontal dashed line shows the inference speed required to match the average speed at which galaxies are being observed across Euclid's 6 year mission, if processed in serial concurrently with detection (Euclid Collaboration et al. 2025). Whilst this is purely illustrative it provides a visual example of the computational challenge of processing such large surveys. We do not include the training data generation or model training time here, since this only has to be performed once for a given configuration, and is not necessary during inference.

overall we see systematically underestimated redshifts, particularly in the  $0 \le z \le 3$  redshift range, which can be seen in the inset histogram. This may be due to a lack of flexibility in our IGM prescription, not accounting for Ly- $\alpha$  emission correctly, or a lack of flexibility in the range of emission line ratios due to our fixed ionisation parameter and gas-phase metallicity.

For comparison the EAZY-py photometric redshifts for the same sample had a outlier fraction  $\eta=0.160$ , an NMAD of 0.04, and a bias of -0.005. The EAZY-py model produces more outliers than synference, but the redshift estimates are less biased with EAZY-py. It is encouraging to see that Model 2 can recover accurate redshifts in the vast majority of cases. Often in the cases where the incorrect photo-z is found, the redshift PDF is bimodal. A more complex model with a variable dust attenuation law slope, 2175Å bump, or variable IGM prescription may shift more of the posterior weight towards the correct solution.

In terms of computation speed, utilizing SBI techniques for only redshift inference is still slower than using EAZY-py in most scenarios. It is somewhat difficult to do a direct comparison between EAZY-py and our SBI model, given the difference in hardware requirements. For fairness our EAZY-py metrics are computed on a single CPU core, but we caution that in reality EAZY-py is likely to be parallelized over multiple cores which will further increase its performance, so this should be taken as a lower limit. However, we can similarly parallelise our inference over multiple cores by copying the trained synference model, and many instances of the trained model could be used in parallel for inference across a large dataset. As shown in Figure 9, our performance metrics show that EAZY-py falls between the speed of the NSF and MDN models, at  $\geq$  50 galaxies/second/core. The strength of the SBI approach to SED fitting is



**Figure 10.** Photometric vs spectroscopic redshift for Model 2 for the JADES spectroscopic catalogue, with the lower panel showing the normalized  $\Delta z/(1+z_s)$  residuals, and an inset panel showing a histogram of  $\Delta z/(1+z_s)$ . Model 2 is slightly biased towards lower redshifts (Bias of -0.043), which may be due to inflexibility in the training dataset (Ly  $\alpha$  emission, DLAs, emission line ratios). The outlier fraction for this sample is 11.7%, many of which are due to Lyman-Balmer confusion.

not the direct comparison to EAZY-py for just photo-z estimation, but the ability to infer accurate posteriors for the physical parameters of the galaxies. Whilst EAZY-py does have some ability to compute estimates of parameters such as stellar mass, SFR, and stellar age based on best-fitting template weights and normalizations, this is not done in a Bayesian framework and does not produce Bayesian posteriors and covariances. A more reasonable speed comparison for SYNFERENCE is Bayesian photometric redshift estimation alongside parameter estimation, e.g. Prospector- $\beta$  (Wang et al. 2023b) or BAG-PIPES with a uniform redshift prior. Prospector- $\beta$  takes >10 hours per fit with nested sampling (Wang et al. 2023b), and when emulated with Parrot (Mathews et al. 2023) this can be reduced to  $\sim$ 30 minutes/galaxy. BAGPIPES can take  $\sim 1-5$  minutes per galaxy to fit using nested sampling, but is somewhat less flexible than PROSPEC-TOR. SYNFERENCE shows a  $10^3 - 10^5$  speed up over the traditional Bayesian approaches to redshift + galaxy parameter inference.

# 6.4 Model Comparison

SED fitting codes are typically built with some limited flexibility around a fundamental set of fixed assumptions. For example, SFH parametrizations and dust attenuation models can often be varied, whilst more fundamental assumptions such as the underlying stellar population model or initial mass function are more difficult to change. With synference the user can be more flexible, as most of the major stellar population synthesis models are supported through synthesizer, along with a variety of IMF parametrizations. Grids with higher dimensionality than just stellar age and metallicity, allowing for direct interpolation across e.g. the IMF high-mass slope,

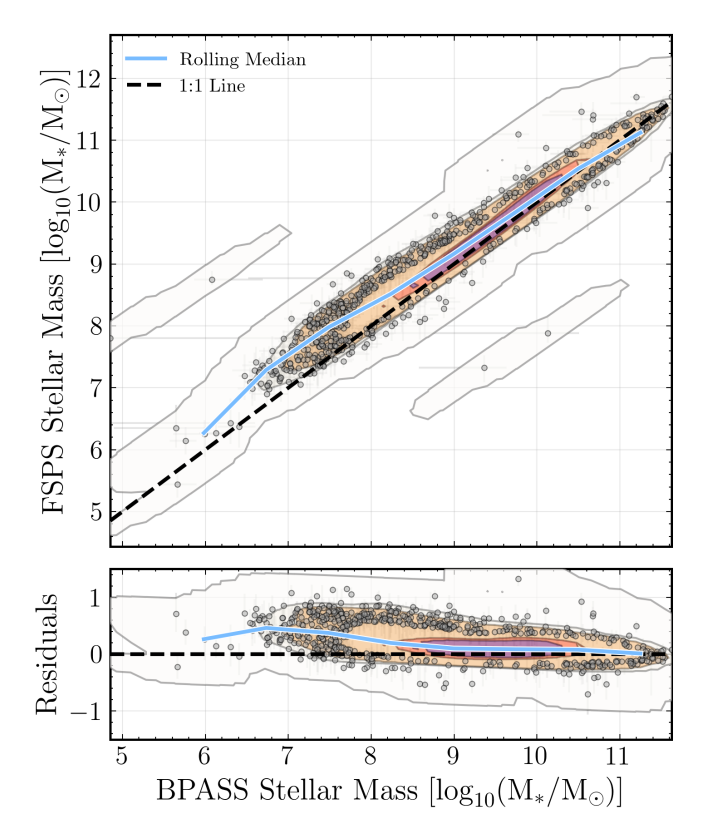


**Figure 11.** Stellar mass comparison between SYNFERENCE models trained on photometry generated from BPASS v2.2.1 SPS grid (Model 1) and a new model trained on photometry from a SPS grid FSPS grids Conroy & Gunn (2010). Both grids use the same Chabrier et al. (2000) IMF. The FSPS grid produces systematically higher stellar mass estimates, especially at  $\log_{10} M_{\star}^{BPASS} < 8$ , with a median offset of 0.3 dex. Most points are contained within the density contours, and only outliers below the 20th percentile of KDE density are plotted as individual points with errorbars.

are also available. Users also have the ability to easily produce and post-process their own custom SPS grids if needed<sup>4</sup>.

This flexibility, along with the speed at which a new model can be trained and used for inference, allows for model selection and comparison, which is difficult to accomplish with a traditional SED fitting approach. As a demonstration of this we have trained a new version of our final model with the same hyperparameters and network architecture, but where we have replaced our BPASS (Stanway & Eldridge 2018) SPS grid with an FSPS (Conroy & Gunn 2010) grid, both with the same Chabrier et al. (2000) IMF and post-processed in the same way. In Figure 11 we show a comparison of the inferred stellar mass between the model using the BPASS SPS grid and the new model constructed from the FSPS grid.

Interestingly, we see that with the same IMF, the FSPS grid produces systematically larger stellar mass estimates. At  $\log_{10} M_{\star}^{BPASS} < 8$  this results in a median offset of 0.3 dex (2×). As both models use the same underlying Chabrier et al. (2000) IMF, this observed mass offset is likely due to differences in the M/L ratios between the two SPS models.

SBI can also be used for explicit Bayesian model comparison and selection, e.g. using evidence ratios (the Bayes factor). There have been a number of studies implementing model comparison within the SBI framework, including Evidence Networks (Jeffrey & Wandelt

2024) and Harmonic Evidence (McEwen et al. 2021; Spurio Mancini et al. 2023). We plan to explore these approaches within SYNFERENCE in future works.

# 6.5 Comparison to Existing Tools

Whilst the application of SBI to SED fitting is relatively new, there have been a few other implementations which we can compare with SYNFERENCE. This includes SBI++ (Wang et al. 2023c) and SBIPIX (Iglesias-Navarro et al. 2025). Both of these approaches have been shown to perform well, with (Wang et al. 2023c) robustly handling missing data and outliers, and (Iglesias-Navarro et al. 2025) optimized for rapid pixel level inference based on a pre-determined model. SYNFERENCE is designed to act as more of a framework, with greater flexibility in the freedom the user has to build and train their model, whereas the existing tools implement a specific SED model and training architecture. SYNFERENCE also enables additional functionality such as hyperparameter optimization, built-in model validation and calibration tests, and SED recovery.

# 6.6 Limitations

Here we address a few of the limitations of the current SYNFERENCE approach. Firstly, there are still some minor inflexibilities in the SYNTHESIZER forward model which will be improved in the future. These include e.g. full support for high-dimensional SPS grids, which will allow e.g. variation in ionisation parameter. This would allow greater flexibility in emission line ratios and strengths for star-forming galaxies.

Overall model performance is another area where improvements may be possible. As discussed in Section 6.1, some parameters, particularly those which are covariant, such as the overall SFH, are not recovered as precisely as traditional SED fitting approaches. Whilst our large hyperparameter optimization has located the optimal configuration for our model, there may be other neural density estimators, approaches such as Neural Score Posterior Estimation (Sharrock et al. 2022) or transformer approaches such as the SIMFORMER (Gloeckler et al. 2024), which may allow us to further improve model performance.

As discussed in Section 2, missing data is an ongoing challenge in applying SBI techniques to real data. All results presented here have utilized only observations where measurements in all filters are available. We have incorporated multiple approaches to dealing with missing data into SYNFERENCE, but we leave a detailed discussion and exploration of these approaches to a future work.

#### 7 SUMMARY AND FUTURE WORK

In this paper we have described SYNFERENCE, a new tool for SED fitting using Simulation-Based Inference. We have demonstrated the performance of SYNFERENCE on a example model, and validated the model on simulated and observed photometry from the JADES GOODS-South field. This tool is built to address the significant computational challenge posed by the immense datasets from current and future surveys like JWST, Roman, and Euclid, for which traditional inference methods are prohibitively slow.

Our main results are summarized as follows:

(i) A New Flexible Framework: synference provides a modular

<sup>&</sup>lt;sup>4</sup> https://github.com/synthesizer-project/grid-generation

and extensible SBI tool for SED fitting. It decouples data simulation (using the flexible SYNTHESIZER package) from neural network training (using the LTU-ILI backend), allowing a single library of simulations to be reused for multiple science applications. Training data can also be generated externally e.g. from forward modelled outputs from hydrodynamical simulations.

- (ii) **Robust Model Training and Validation**: We detailed our process for feature engineering, empirical noise modelling, and hyperparameter optimisation using Optuna, which identified a Neural Spline Flow (NSF) as the optimal architecture for our problem. We rigorously validated our fiducial 8-parameter model, Model 1, against a held-out test set and reference posteriors from Dynesty. The model demonstrates excellent parameter recovery ( $R^2 = 0.99$  for  $M_{\star}$ ,  $R^2 = 0.86$  for  $A_V$ ) and reliable posterior calibration, passing all TARP and coverage tests.
- (iii) **Exceptional Inference Speed**: We applied Model 1 to a sample of 3,088 galaxies with spectroscopic redshifts in the JADES GOODS-South field. The amortized inference for the entire sample took ~ minutes on a desktop CPU, a speedup of ~1700× compared to the ~80 CPU-hours required for an equivalent analysis with the SED fitting code BAGPIPES.
- (iv) Accurate Application to Real Data: The physical properties inferred by SYNFERENCE show good agreement with those from BAGPIPES. We found that SYNFERENCE was more robust in fitting quiescent galaxies where BAGPIPES struggled to find the correct solution, highlighting the ability of NPE to handle complex posterior landscapes.
- (v) **Expanded Capabilities**: We demonstrated the power of SYNFERENCE for applications beyond standard SED fitting. By training a model to infer redshift (Model 2), we showed it can produce full Bayesian posteriors for both redshift and physical parameters at a speed  $10^3 10^5 \times$  faster than traditional Bayesian methods. We also highlighted its use for rapid model comparison by training a new model with a the FSPS SPS model (instead of BPASS) and quantifying the systematic 0.3 dex offset in stellar mass.

SYNFERENCE provides a scalable and powerful solution for exploiting the next generation of astronomical surveys, enabling fast, full-posterior inference for billions of galaxies. We plan to apply SYNFERENCE in numerous contexts in future work, including in spatially resolved galaxy studies, inference from hydrodynamical simulations, Bayesian model comparison, and high-dimensional inference from spectroscopy.

# **ACKNOWLEDGEMENTS**

TH, CC, NA, DA, QL, VR, KM, acknowledge support from the ERC Advanced Investigator Grant EPOCHS (788113), as well as two studentships from the STFC. CCL was supported by the research environment and infrastructure of the Handley Lab at the University of Cambridge. WJR, APV and SMW acknowledge support from the Sussex Astronomy Centre STFC Consolidated Grant (ST/X001040/1). PIN thanks the LSST-DA Data Science Fellowship Program, which is funded by LSST-DA, the Brinson Foundation, the WoodNext Foundation, and the Research Corporation for Science Advancement Foundation; her participation in the program has benefited this work. PIN acknowledge financial support from the State

Research Agency of the Spanish Ministry of Science and Innovation (AEI-MCINN) under the grants "Galaxy Evolution with Artificial Intelligence" with reference PGC2018-100852-A-I00 and "BASALT" with reference PID2021-126838NB-I00. All contributions from NA were made before he left academia.

This work is based on observations made with the NASA/ESA *Hubble Space Telescope* (HST) and NASA/ESA/CSA *James Webb Space Telescope* (JWST) obtained from the Mikulski Archive for Space Telescopes (MAST) at the *Space Telescope Science Institute* (STScI), which is operated by the Association of Universities for Research in Astronomy, Inc., under NASA contract NAS 5-03127 for JWST, and NAS 5-26555 for HST.

This work used the DiRAC@Durham facility managed by the Institute for Computational Cosmology on behalf of the STFC DiRAC HPC Facility (www.dirac.ac.uk). The equipment was funded by BEIS capital funding via STFC capital grants ST/P002293/1, ST/R002371/1 and ST/S002502/1, Durham University and STFC operations grant ST/R000832/1. DiRAC is part of the National e-Infrastructure.

# DATA AVAILABILITY

The SYNFERENCE package used to generate the training data and train the SBI models is available on GitHub at https://github.com/synthesizer-project/synference. Documentation for using synFerence is available at https://synthesizer-project.github.io/synference.synThesizer is also available on GitHub at https://github.com/synthesizer-project/synthesizer. Model 1 is available to download through the synference-download tool built into the package, and we plan to distribute more pre-trained models in future works

The EPOCHS JADES catalogue and imaging are available upon reasonable request to the corresponding author, and will be made public as part of the EPOCHS-v2 project (Austin et al. in prep.).

### REFERENCES

Adams N. J., et al., 2024, ApJ, 965, 169

Aggarwal C. C., et al., 2015, Data mining: the textbook. Vol. 1, Springer Akiba T., Sano S., Yanase T., Ohta T., Koyama M., 2019, in Proceedings of the 25th ACM SIGKDD international conference on knowledge discovery & data mining. pp 2623–2631

Alsing J., Charnock T., Feeney S., Wandelt B., 2019, MNRAS, 488, 4440 Alsing J., et al., 2020, ApJS, 249, 5

Alvey J., Contaldi C. R., Pieroni M., 2025, Simulation-Based Inference with Deep Ensembles: Evaluating Calibration Uncertainty and Detecting Model Misspecification (arXiv:2507.13495), doi:10.48550/arXiv.2507.13495

Angiulli F., Pizzuti C., 2002, in European conference on principles of data mining and knowledge discovery. pp 15–27

Asada Y., et al., 2025, ApJ, 983, L2

Asadi V., Zonoozi A. H., Haghi H., Abedini F., Kalantari A., Jafariyazani M., Chartab N., 2025, ApJ, 989, 65

Aufort G., et al., 2024, Reconstructing Galaxy Star Formation Histories from COSMOS2020 Photometry Using Simulation-Based Inference, doi:10.48550/arXiv.2410.00795

Austin D., et al., 2024, arXiv e-prints, p. arXiv:2404.10751

Bacon R., et al., 2010, in Ground-based and airborne instrumentation for astronomy III. pp 131–139

Bacon R., et al., 2023, A&A, 670, A4

Bairagi A., Wandelt B., Villaescusa-Navarro F., 2025, arXiv preprint arXiv:2503.13755 Berger S., Marshall M. A., Wyithe J. S. B., di Matteo T., Ni Y., Wilkins S. M., Yue M., 2025, Biases in Stellar Masses of JWST High-z Quasar Host Galaxies Caused by Quasar Subtraction (arXiv:2506.12130), doi:10.48550/arXiv.2506.12130

Bishop C. M., 1994

Boelts J., et al., 2024, arXiv preprint arXiv:2411.17337

Bradbury J., et al., 2021, Astrophysics Source Code Library, pp ascl-2111

Brammer G. B., van Dokkum P. G., Coppi P., 2008, ApJ, 686, 1503

Brammer G. B., et al., 2012, ApJS, 200, 13

Brooks R. A. N., Sanders J. L., Chandra V., Garavito-Camargo N., Dillamore A. M., Price-Whelan A. M., Ting Y.-S., 2025, arXiv e-prints, p. arXiv:2510.04735

Bruzual G., Charlot S., 2003, MNRAS, 344, 1000

Bunker A. J., et al., 2023, arXiv e-prints, p. arXiv:2306.02467

Calzetti D., Armus L., Bohlin R. C., Kinney A. L., Koornneef J., Storchi-Bergmann T., 2000, ApJ, 533, 682

Camps P., Baes M., 2015, Astronomy and Computing, 9, 20

Cannon P., Ward D., Schmon S. M., 2022, Investigating the Impact of Model Misspecification in Neural Simulation-based Inference (arXiv:2209.01845), doi:10.48550/arXiv.2209.01845

Carnall A. C., McLure R. J., Dunlop J. S., Davé R., 2017, MNRAS, 480, 4379

Carnall A. C., Leja J., Johnson B. D., McLure R. J., Dunlop J. S., Conroy C., 2019, ApJ, 873, 44

Casey C. M., 2012, MNRAS, 425, 3094

Chabrier Gilles 2003, PASP, 115, 763

Chabrier G., Baraffe I., Allard F., Hauschildt P., 2000, ApJ, 542, 464

Charlot S., Fall S. M., 2000, ApJ, 539, 718

Chen R. T., Rubanova Y., Bettencourt J., Duvenaud D. K., 2018, Advances in neural information processing systems, 31

Chen H., Speagle J., Rogers K. K., 2023, Learning Reionization History from Quasars with Simulation-Based Inference (arXiv:2311.16238), doi:10.48550/arXiv.2311.16238

Choustikov N., Stiskalek R., Saxena A., Katz H., Devriendt J., Slyz A., Subdepartment of Astrophysics U. o. O., 2025, MNRAS, 537, 2273

Ćiprijanović A., et al., 2021, MNRAS, 506, 677

Collister A. A., Lahav O., 2004, PASP, 116, 345

Conroy C., Gunn J. E., 2010, Astrophysics Source Code Library, pp ascl–1010 Conselice C. J., et al., 2025, ApJ, 983, 30

Cook S. R., Gelman A., Rubin D. B., 2006, Journal of Computational and Graphical Statistics, 15, 675

Crain R. A., et al., 2015, MNRAS, 450, 1937

Cranmer K., Brehmer J., Louppe G., 2020, Proceedings of the National Academy of Sciences, 117, 30055

D'Eugenio F., et al., 2025, ApJS, 277, 4

Davidzon I., et al., 2022, A&A, 665, A34

Deger S., Peiris H. V., Thorp S., Mortlock D. J., Jagwani G., Alsing J., Leistedt B., Leja J., 2025, arXiv e-prints, p. arXiv:2509.20430

Deistler M., Goncalves P. J., Macke J. H., 2022, Advances in neural information processing systems, 35, 23135

Developers T., 2022, Zenodo

Dobbels W., Krier S., Pirson S., Viaene S., De Geyter G., Salim S., Baes M., 2019, Astronomy & Astrophysics, 624, A102

Doré O., et al., 2014, arXiv e-prints, p. arXiv:1412.4872

Draine B. T., Li A., 2007, ApJ, 657, 810

Durkan C., Bekasov A., Murray I., Papamakarios G., 2019, Neural Spline Flows (arXiv:1906.04032), doi:10.48550/arXiv.1906.04032

Durkan C., Murray I., Papamakarios G., 2020, On Contrastive Learning for Likelihood-free Inference (arXiv:2002.03712), doi:10.48550/arXiv.2002.03712

Eisenstein D. J., et al., 2023a, arxiv

Eisenstein D. J., et al., 2023b, arXiv e-prints, p. arXiv:2306.02465

Euclid Collaboration et al., 2025, A&A, 697, A1

Ferland G. J., et al., 2017, Rev. Mex. Astron. Astrofis., 53, 385

Feroz F., Hobson M., Bridges M., 2009, MNRAS, 398, 1601

Firth A. E., Lahav O., Somerville R. S., 2003, MNRAS, 339, 1195

Fischbacher S., Moser B., Kacprzak T., Herbel J., Tortorelli L., Schmitt U.,

Refregier A., Amara A., 2025, Journal of Open Source Software, 10, 8766

Frontera-Pons J., Sureau F., Bobin J., Le Floc'h E., 2017, A&A, 603, A60 Gardner J. P., et al., 2006, Space Sci. Rev., 123, 485

Gelman A., 2006

Germain M., Gregor K., Murray I., Larochelle H., 2015, in International conference on machine learning. pp 881–889

Gilda S., Lower S., Narayanan D., 2021, ApJ, 916, 43

Gloeckler M., Deistler M., Weilbach C., Wood F., Macke J. H., 2024, All-in-One Simulation-Based Inference (arXiv:2404.09636), doi:10.48550/arXiv.2404.09636

Grathwohl W., Chen R. T., Bettencourt J., Sutskever I., Duvenaud D., 2018, arXiv preprint arXiv:1810.01367

Greenberg D. S., Nonnenmacher M., Macke J. H., 2019, Automatic Posterior Transformation for Likelihood-Free Inference (arXiv:1905.07488), doi:10.48550/arXiv.1905.07488

Griesemer S., Cao D., Cui Z., Osorio C., Liu Y., 2024, Advances in Neural Information Processing Systems, 37, 127907

Gunes B., Buder S., Buck T., 2025, arXiv preprint arXiv:2507.05060

Hahn C., Melchior P., 2022, ApJ, 938, 11

Hahn C., Bottrell C., Lee K.-G., 2024, ApJ, 968, 90

Hainline K. N., et al., 2024, ApJ, 964, 71

Harvey T., et al., 2025a, MNRAS, 542, 2998

Harvey T., et al., 2025b, ApJ, 978, 89

He Z., Xu X., Deng S., 2003, Pattern recognition letters, 24, 1641

Hemmati S., et al., 2019, ApJ, 881, L14

Hermans J., Begy V., Louppe G., 2020, Likelihood-Free MCMC with Amortized Approximate Ratio Estimators (arXiv:1903.04057), doi:10.48550/arXiv.1903.04057

Hermans J., Delaunoy A., Rozet F., Wehenkel A., Begy V., Louppe G., 2021, arXiv preprint arXiv:2110.06581

Ho M., et al., 2024, arXiv preprint arXiv:2402.05137

Iglesias-Navarro P., Huertas-Company M., Martín-Navarro I., Knapen J. H., Pernet E., 2024, Astronomy & Astrophysics, 689, A58

Iglesias-Navarro P., et al., 2025, Simulation-Based Inference of Galaxy Properties from JWST Pixels (arXiv:2506.04336), doi:10.48550/arXiv.2506.04336

Illingworth G., et al., 2016, arXiv e-prints, p. arXiv:1606.00841

Inoue A. K., Shimizu I., Iwata I., Tanaka M., 2014, MNRAS, 442, 1805 Ivezić Ž., et al., 2019, ApJ, 873, 111

Iyer K. G., Gawiser E., Faber S. M., Ferguson H. C., Kartaltepe J., Koekemoer A. M., Pacifici C., Somerville R. S., 2019, ApJ, 879, 116

Iyer K. G., et al., 2020, MNRAS, 498, 430

Iyer K. G., Speagle J. S., Caplar N., Forbes J. C., Gawiser E., Leja J., Tacchella S., 2024, ApJ, 961, 53

Jakobsen P., et al., 2022, A&A, 661, A80

Jeffrey N., Wandelt B. D., 2024, Machine Learning: Science and Technology, 5, 015008

Jeffrey N., et al., 2025, MNRAS, 536, 1303

Johnson B. D., Leja J., Conroy C., Speagle J. S., 2020, ApJS, 254, 22

Khullar G., Nord B., Ćiprijanović A., Poh J., Xu F., 2022, Machine Learning: Science and Technology, 3, 04LT04

Kingma D. P., Ba J., 2014, arXiv preprint arXiv:1412.6980

Kobyzev I., Prince S. J. D., Brubaker M. A., 2021, IEEE Transactions on Pattern Analysis and Machine Intelligence, 43, 3964

Kubota A., Done C., 2018, MNRAS, 480, 1247

Kullback S., Leibler R. A., 1951, The annals of mathematical statistics, 22,

Kurk J., et al., 2013, Astronomy & Astrophysics, 549, A63

Latecki L. J., Lazarevic A., Pokrajac D., 2007, in International workshop on machine learning and data mining in pattern recognition. pp 61–75

Lazarevic A., Kumar V., 2005, in Proceedings of the eleventh ACM SIGKDD international conference on Knowledge discovery in data mining. pp 157–

Le Fèvre O., et al., 2004, A&A, 428, 1043

Leja J., Johnson B. D., Conroy C., Van Dokkum P. G., Byler N., 2017, ApJ, 837, 170 Leja J., Carnall A. C., Johnson B. D., Conroy C., Speagle J. S., 2019, ApJ, 876.3

Lemos P., Coogan A., Hezaveh Y., Perreault-Levasseur L., 2023, in International Conference on Machine Learning. pp 19256-19273

Li A., Liang S., Kann D., Wei D., Klose S., Wang Y., 2008, ApJ, 685, 1046 Li Z., Zhao Y., Hu X., Botta N., Ionescu C., Chen G. H., 2022, IEEE Transactions on Knowledge and Data Engineering, 35, 12181

Li J., Melchior P., Hahn C., Huang S., 2024, AJ, 167, 16

Liu F. T., Ting K. M., Zhou Z.-H., 2008, in 2008 eighth ieee international conference on data mining. pp 413-422

Lopez-Paz D., Oquab M., 2016, arXiv preprint arXiv:1610.06545

Lovell C. C., Acquaviva V., Thomas P. A., Iyer K. G., Gawiser E., Wilkins S. M., 2019, MNRAS, 490, 5503

Lovell C. C., et al., 2024, arXiv preprint arXiv:2411.13960

Lovell C. C., Roper W. J., Vijayan A. P., Wilkins S. M., Newman S., Seeyave L., 2025, Synthesizer: a Software Package for Synthetic Astronomical Observables (arXiv: 2508.03888), https://arxiv.org/abs/2508.

Lueckmann J.-M., Boelts J., Greenberg D. S., Gonçalves P. J., Macke J. H., 2021, Benchmarking Simulation-Based Inference (arXiv:2101.04653), doi:10.48550/arXiv.2101.04653

Lupton R., Blanton M. R., Fekete G., Hogg D. W., O'Mullane W., Szalay A., Wherry N., 2004, Publications of the Astronomical Society of the Pacific, 116, 133

Madau P., 1995, ApJ, 441, 18

Maraston C., 2005, MNRAS, 362, 799

Mathews E. P., et al., 2023, ApJ, 954, 132

McEwen J. D., Wallis C. G. R., Price M. A., Docherty M. M., 2021, ArXiv McKay M. D., Beckman R. J., Conover W. J., 2000, Technometrics, 42, 55

Mediato-Diaz N., Handley W., 2025, arXiv preprint arXiv:2501.03921

Modi C., Pandey S., Ho M., Hahn C., Blancard B. R.-S., Wandelt B., 2023, Sensitivity Analysis of Simulation-Based Inference for Galaxy Clustering (arXiv:2309.15071), doi:10.48550/arXiv.2309.15071

Momcheva I. G., et al., 2016, ApJS, 225, 27

Moser B., Kacprzak T., Fischbacher S., Refregier A., Grimm D., Tortorelli L., 2024, J. Cosmology Astropart. Phys., 2024, 049

Newman J. A., Gruen D., 2022, Annual Review of Astronomy and Astrophysics, 60, 363

Newman S. L., Lovell C. C., Maraston C., Roper W. J., Vijayan A. P., Wilkins S. M., Giavalisco M., Saxena A., 2025, MNRAS,

Papamakarios G., Pavlakou T., Murray I., 2018, Masked Autoregressive Flow for Density Estimation (arXiv:1705.07057), doi:10.48550/arXiv.1705.07057

Papamakarios G., Sterratt D. C., Murray I., 2019, Sequential Neural Likelihood: Fast Likelihood-free Inference with Autoregressive Flows (arXiv:1805.07226), doi:10.48550/arXiv.1805.07226

Papamakarios G., Nalisnick E., Rezende D. J., Mohamed S., Lakshminarayanan B., 2021, Journal of Machine Learning Research, 22, 1

Paszke A., et al., 2019, Advances in neural information processing systems,

Pillepich A., et al., 2018, MNRAS, 473, 4077

Rieke M. J., et al., 2023a, arxiv

Rieke M. J., et al., 2023b, ApJS, 269, 16

Rodrigo C., Solano E., 2020, The SVO Filter Profile Service. https://ui. adsabs.harvard.edu/abs/2020sea..confE.182R

Rodrigo C., Solano E., Bayo A., 2012, Technical report, SVO Filter Profile Service Version 1.0, https://ui.adsabs.harvard.edu/abs/ 2012ivoa.rept.1015R, doi:10.5479/ADS/bib/2012ivoa.rept.1015R., https://ui.adsabs.harvard.edu/abs/2012ivoa.rept.1015R

Roper W. J., et al., 2025, arXiv preprint arXiv:2506.15811

Salvato M., Ilbert O., Hoyle B., 2019, Nature Astronomy, 3, 212

Sante A., Kawata D., Font A. S., Grand R. J. J., 2025, MNRAS, 542, 1776 Schaye J., et al., 2015, MNRAS, 446, 521

Sharrock L., Simons J., Liu S., Beaumont M., 2022, arXiv preprint arXiv:2210.04872

Skelton R. E., et al., 2014, ApJS, 214, 24

Spergel D., et al., 2015, arXiv e-prints, p. arXiv:1503.03757

Spurio Mancini A., Docherty M. M., Price M. A., McEwen J. D., 2023, RAS Techniques and Instruments, 2, 710

Stanway E. R., Eldridge J., 2018, MNRAS, 479, 75

Suess K. A., et al., 2022, ApJ, 935, 146

Surana S., Wadadekar Y., Bait O., Bhosale H., 2020, MNRAS, 493, 4808 Tacchella S., et al., 2022, ApJ, 927, 170

Talts S., Betancourt M., Simpson D., Vehtari A., Gelman A., 2018, arXiv preprint arXiv:1804.06788

Tejero-Cantero A., Boelts J., Deistler M., Lueckmann J.-M., Durkan C., Gonçalves P. J., Greenberg D. S., Macke J. H., 2020, arXiv preprint arXiv:2007.09114

Thorp S., Alsing J., Peiris H. V., Deger S., Mortlock D. J., Leistedt B., Leja J., Loureiro A., 2024, ApJ, 975, 145

Thorp S., et al., 2025, Pop-Cosmos: Insights from Generative Modeling of a Deep, Infrared-Selected Galaxy Population (arXiv:2506.12122), doi:10.48550/arXiv.2506.12122

Tony L. F., Ming T. K., Zhi-Hua Z., 2012, ACM Transactions on Knowledge Discovery from Data (TKDD), 6, 3

Vanzella E., et al., 2005, A&A, 434, 53

Vanzella E., et al., 2006, A&A, 454, 423

Vanzella E., et al., 2008, A&A, 478, 83

Vanzella E., et al., 2009, ApJ, 695, 1163

Vincent P., 2011, Neural computation, 23, 1661

Wan J. T., Tacchella S., Johnson B. D., Iyer K. G., Speagle J. S., Maiolino R., 2024, MNRAS, 532, 4002

Wang B., Leja J., Villar A., Speagle J. S., 2022, Monte Carlo Techniques for Addressing Large Errors and Missing Data in Simulation-based Inference (arXiv:2211.03747), doi:10.48550/arXiv.2211.03747

Wang B., et al., 2023a, ApJS, 270, 12

Wang B., et al., 2023b, ApJ, 944, L58

Wang B., Leja J., Villar V. A., Speagle J. S., 2023c, ApJ, 952, L10

Wang Z., Hasenauer J., Schälte Y., 2024, PLOS Computational Biology, 20, e1012184

Weaver J. R., et al., 2024, ApJS, 270, 7

Weibel A., et al., 2024, MNRAS, 533, 1808

Whitaker K. E., et al., 2019, ApJS, 244, 16

Widmark A., Johnston K. V., 2025, Using Simulation Based Inference on Tidally Perturbed Dwarf Galaxies: The Dynamics of NGC205 (arXiv:2501.13148), doi:10.48550/arXiv.2501.13148

Xu H., Pang G., Wang Y., Wang Y., 2023, IEEE Transactions on Knowledge and Data Engineering, 35, 12591

Yuan J., Zaw I., Nemer A., Chen Y., 2025, in American Astronomical Society Meeting Abstracts #245. p. 359.02

Zackrisson E., Rydberg C.-E., Schaerer D., Östlin G., Tuli M., 2011, ApJ, 740, 13

Zhao Y., Nasrullah Z., Li Z., 2019, Journal of machine learning research, 20,

Zhao D., Dalmasso N., Izbicki R., Lee A. B., 2021, in Uncertainty in Artificial Intelligence. pp 1830-1840

Zubeldia I., Bolliet B., Challinor A., Handley W., 2025, arXiv preprint arXiv:2504.10230

#### APPENDIX A: ACCURACY OF BAGPIPES INFERENCE

In Section 5.5 we compare galaxy properties inferred with SYNFER-ENCE to the results of the standard BAGPIPES Bayesian SED fitting tool. However given that this comparison is done on a catalogue of real galaxies, rather than mock data, we do not have access to the ground truth to assess the absolute performance of either tool. Whilst we assess the accuracy and reliability of SYNFERENCE in Section 4.4, we do not validate whether BAGPIPES itself can accurately recover model parameters. In this appendix we test BAGPIPES using the same validation dataset we use for synference.

We randomly draw 1000 galaxies from the subset of the validation dataset for Model 1 which has average SNR > 5 in F277W, F356W

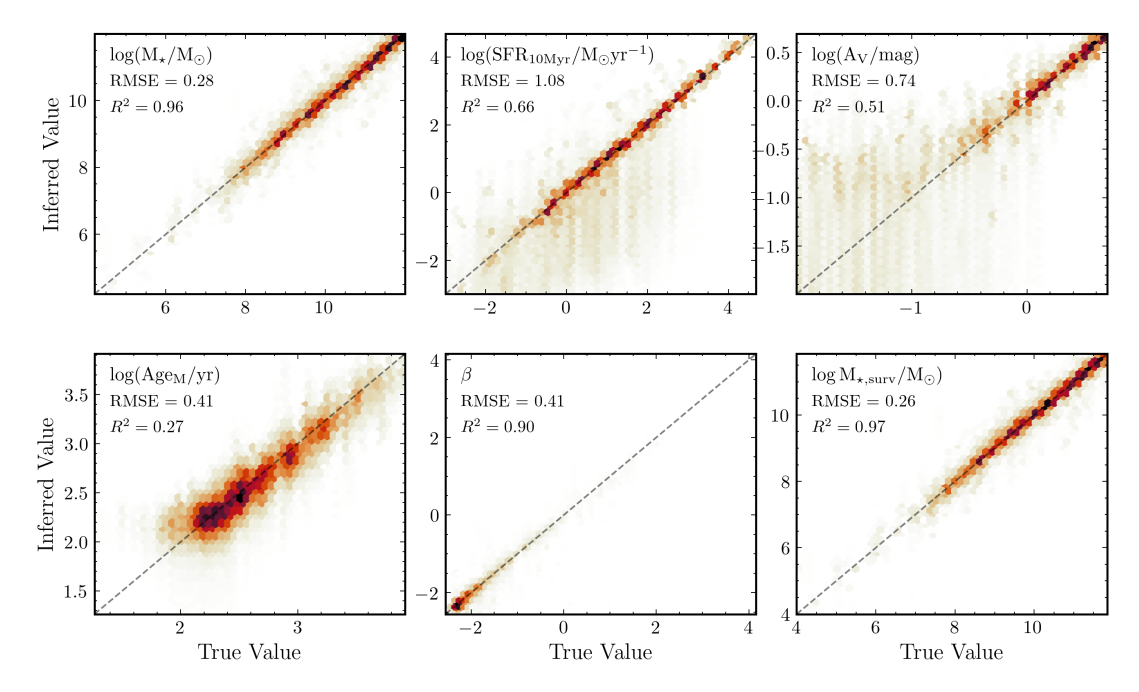


**Figure A1.** Equivalent of Figure 4 for BAGPIPES, showing model performance on  $\geq 5\sigma$  validation set.

and F444W. We fit these galaxies using BAGPIPES in the same way as described in Section 5.5. We compute  $R^2$  and RMSE in the same method as for SYNFERENCE.

Figure A1 shows the equivalent of Figure 4 for the equivalent BAGPIPES results as determined by comparing the ground-truth of the validation dataset to the results of BAGPIPES fitting. The BAGPIPES model is less accurate and more biased than the SYNFERENCE model. The figure shows the  $R^2$  and RMSE values for each parameter. The RMSE errors for these parameters using BAGPIPES are lower than or comparable to Model 1 for the same subset of the validation dataset, which can be compared with Table 4. This suggests that SYNFERENCE can produce results which are more accurate than BAGPIPES.

This paper has been typeset from a  $\ensuremath{\text{TEX/IATeX}}$  file prepared by the author.